DEVELOPMENT OF CERIA-ZIRCONIA NANOCOMPOSITES FOR CATALYTIC CRACKING OF HYDROCARBONS

BY

OLUWOLE OLAGOKE AJUMOBI

A Thesis Presented to the
DEANSHIP OF GRADUATE STUDIES

KING FAHD UNIVERSITY OF PETROLEUM & MINERALS

DHAHRAN, SAUDI ARABIA

In Partial Fulfillment of the
Requirements for the Degree of

MASTER OF SCIENCE

In

CHEMICAL ENGINEERING

MAY, 2017

KING FAHD UNIVERSITY OF PETROLEUM & MINERALS

DHAHRAN- 31261, SAUDI ARABIA

DEANSHIP OF GRADUATE STUDIES

This thesis, written by **Oluwole Olagoke AJUMOBI** under the direction his thesis advisor and approved by his thesis committee, has been presented and accepted by the Dean of Graduate Studies, in partial fulfillment of the requirements for the degree of **MASTER OF SCIENCE IN CHEMICAL ENGINEERING**.

A. Al Amer

Dr. Adnan Al-Amer
(Advisor)

Oki Muraza

Dr. Dr. Oki Muraza
(Co-Advisor)

Dr. Mohammed S. Ba-Shammakh
Department Chairman

Mozzhar Hossain

Dr. Mohammad M. Hossain
(Member)

Dr. Salam A. Zummo
Dean of Graduate Studies

عمادة الدراسات العليا
DEANSHIP OF GRADUATE STUDIES

8/5/17

Date

Dr. Zuhair O. Malaibari
(Member)

Shaikh Abdur Razzak

Dr. Shaikh Abdur Razaq
(Member)

I dedicate the beginning and completion of this work to the Almighty God and in loving memory of my late mother, Mrs. Ninyo Ajumobi

ACKNOWLEDGMENTS

I will like to thank the funding provided by Saudi Aramco for supporting this work through project contract number 6600011900 as part of the Oil Upgrading theme at King Fahd University of Petroleum and Minerals. My appreciation goes to my advisor Dr. Adnan Al-amer and my co-advisor, Dr. Oki Muraza. I will also like to show appreciation to the committee members (Dr M. Hossain, Dr Abdur Razaq and Dr Malaibari) for their advice, guidance, supports, comments and suggestions towards making this research work more comprehensive and professional. I will also like to appreciate the effort of Mr. Idris A. Bakare on his effort in tutoring and usage of characterization equipment (x-ray diffraction, temperature-programmed desorption, Fourier transform infrared spectroscopy, among others, for the actualization and completion this work. I also want to acknowledge the contribution from S. Adewale for Raman spectroscopy analysis, M. Qamaruddin on the analysis of textural properties, and Mr. Teguh for catalytic testing reactor.

TABLE OF CONTENTS

LIST OF TABLES

LIST OF FIGURES

LIST OF ABBREVIATIONS

CZ:	Ceria-zirconia nanocomposite (25 wt.% Zr and 75 wt.% Ce)
CoCZ:	cobalt-doped ceria-zirconia nanocomposite (20 wt.% Co, 20 wt.% Zr and 60 wt.% Ce)
FeCZ:	iron-doped ceria-zirconia nanocomposite (20 wt.% Fe, 20 wt.% Zr and 60 wt.% Ce)
FeCoCZ_A:	Iron, cobalt co-doped ceria-zirconia nanocomposite (10 wt.% Fe, 10 wt.% Co, 20 wt.% Zr and 60 wt.% Ce)
FeCoCZ_B:	Iron, cobalt co-doped ceria-zirconia nanocomposite (5 wt.% Fe, 5 wt.% Co, 20 wt.% Zr and 70 wt.% Ce)
TFE:	Teflon
BJH:	Barrett-Joyner-Halenda
XRD:	X-ray Diffractometer
FE-SEM:	Field Emission Scanning Electron Microscopy
BET:	Braunnaeur_Emmett_Teller
FT-IR:	Fourier Transform Infrared Radiation
TGA:	Themogravimetric Analysis
TOS:	Time-on-stream

ABSTRACT

Full Name : [Oluwole Olagoke Ajumobi]

Thesis Title : [Development of Ceria-Zirconia Nanocomposites for Catalytic Cracking of Hydrocarbons]

Major Field : [Chemical Engineering]

Date of Degree : [May 2017]

Nano-sized iron- and cobalt-doped ceria-zirconia nanocomposites were synthesized via hydrothermal synthesis technique at 180 °C for 8 - 24 h, with the novel incorporation of both Co and Fe into ceria-zirconia (CZ), for n-hexane catalytic cracking. The intrinsic properties of ceria-zirconia were investigated using different characterization techniques. Influence of dopant ions on the improvement of basic properties of ceria-zirconia nanocomposites were also studied. Ceria-zirconia and its doped nanocomposites showed similar x-ray diffraction (XRD) patterns and significant to full fusion of the metal/dopant ions into the ceria-zirconia lattice structure. The prepared nanocomposite catalysts were tested for n-hexane cracking for 10 h time-on-stream. It should be noted that there has been no previous report or study on catalytic cracking of hexane via ceria-zirconia nanocomposites, highlighting the novelty of this application. Appreciably high ethylene and propylene selectivity, each > 31%, was obtained over CZ, FeCoCZ_A and FeCoCZ_B at the stipulated time-on-stream. Comparatively, FeCoCZ_A exhibited the best catalytic activity and stability with higher n-hexane conversions (49% at 1 h and 33% after 10 h) over time-on-stream. Temperature and time factor (W/F) variations were carried out on the best catalyst (FeCoCZ_A). Higher conversions were evaluated at higher reaction temperature and lower W/F. In addition, the spent catalysts were successfully regenerated

via thermal approach by calcining the spent samples at 600 °C for 4 h. The regenerated samples were tested, repeating the regeneration and reusability procedure for two additional cycles. The XRD and scanning electron microscopy characterization results showed that the morphology (shape, phase structure and size) of the samples were restored after regeneration. Also, the regenerated samples were tested and exhibited catalytic activity for hexane cracking, with 9.1 % and 16.9 % loss in conversion after the first and second regeneration cycle, respectively.

ملخص الرسالة

الاسم الكامل: البركة أولاغوك أجوموبي

عنوان الرسالة: تطوير سيريا زيركونيا نانوكومبوسيتس للتكسير التحفيزي للهيدروكربونات

التخصص: هندسة كيميائية

تاريخ الدرجة العلمية: مايو 2017

الهيدرو حراري عند 180 درجة مئوية لمدة تتراوح مابين 8- 24 ساعة، وتم استخدام المادة المصنعة كمادة محفزة في تفاعل تكسير مركب الهكسان، حيث تم استخدام العديد من التقنيات لمعرفة خصائص المادة المصنعة. تأثير كلا من الحديد والكوبلت في تحسين الخصائص الاساسية لصفيحة الزركونيا والسيريا النانوية كذلك تم دراستها، وأظهرت نتائج الاشعة السينية (XRD) بإن نتائج كلا من الصفيحة الأم و المطعمة بمركبي الحديد والكوبلت متشابهة تماما. بالنسبة لاختبار المادة النانونية المصنعة في تكسير الهكسان تم اختبارها لمدة 10 ساعات. وجب التذكير بانه لم يسبق قط استخدام صفيحة الزركونيا والسيريا النانوية في هذا التفاعل مما يجعل هذا البحث فريد من نوعه. اظهرت النتائح بشكل ملحوظ ان اختيارية المادة لمركبي الايثيلين والبروبيلين كانت اكثر من 30% لصفيحة الزركونيا والسيريا و بعد تطعيمهما بالحديد والكوبلت عند الزمن المنصوص سابقا. وللمقارنه، الصفيحة المطعمة بالحديد كانت اكثر فعالية واستقرارا، حيث كانت نسبة تحول الهكسان 49% بعد ساعة من بدأ التفاعل و 33% بعد 10 ساعات من بدا التفاعل. بعد ذلك تم اختبار تاثير درجة الحرارة ونسبة وزن المادة المحفزة لمعدل التدفق على المادة التي اظهرت افضل فعالية وهي المادة المطعمة بالحديد. نسبة تحول اعلى للهكسان تم اختباره عند درجة حرارة عالية و عند نسبة اقل لوزن المادة لمعدل التدفق. اضافة انه تم بنجاح اعادة تنشيط المادة بعد ان فقدت فعاليتها عن طريق التسخين عند 600 درجة مئوية لمدة 4 ساعات، حيث تم استخدام المادة مجدد في التفاعل واعادة تنشيطة لدورتين اخرى. اظهرت نتائج الاشعة السينية وكذلك المجهر الالكتروني بان خصائص المادة (كالشكل والتركيب والحجم) بعد التنشيد لم تفقد. كذلك تم اختبار المادة المنشطة في التفاعل حيث انها فقدت 9.1% من تحول الهكسان بعد التنشيط الاول و 16.9% بعد الدورة الثانية من التنشيط.

CHAPTER 1

INTRODUCTION

1.1 Background Information

The use of mixed metallic oxides is known to have several applications in the field of science. Their applicability has been stretched to the area of catalysis. These oxides are now being used as catalysts for different purposes such as cracking of crude oil or enhancing the economics and processing phenomena of diverse production processes.

The most crucial needs for production in the world today is rapid chemical reaction processes and energy. This has attracted the attention of scientists, engineers and researchers to develop several ways of obtaining fuels, especially from crude oil sources via catalytic cracking. The use of ceria and ceria-based composites have gained enormous recognition in recent times due to the ability of these ceria and ceria-based composite catalysts to catalyse the cracking of heavy oils, as a Three-Way Catalyst (TWC) for reduction of pollutant gases (NOx, CO and hydrocarbons) from automobile exhaust [1]–[7], Water-Gas Shift processes (WGS) [4], CO and soot oxidation reaction [4], [8]–[17] etc. Ceria and ceria-based composites are known to have a high OSC [16]–[21], making them more valuable for cracking of heavy oil components along with their stability in harsh reaction media. Thus, these catalysts can perform reduction-oxidation (red-ox) reactions

during catalytic processes due to the ability of cerium ions to exist in Ce^{3+}/Ce^{4+} oxidation states.

Several methods are available for the synthesis of ceria-zirconia (CeO_2-ZrO_2) composite oxides such as sol-gel technique, hydrothermal synthesis in Supercritical water (SCW), Electrospinning to obtain nanofibers, microwave method, precipitation, and so on. The characteristics and catalytic performance of any synthesized ceria (CeO_2) composite oxides depend on the synthesis method and medium. Doping ceria (cerium oxide) with particular transition metals (such as zirconium, iron and cobalt) and rare earth metals (e.g. yttrium), improve the OSC and stability of ceria, especially in harsh reaction environment.

1.2 Hydrocarbon Cracking for Production of Light Olefins

Light olefins are known to be significant raw materials needed for production of plastics and other petrochemical products. The demand for ethylene and propylene around the world is increasing steadily. These olefins are commonly produced from steam cracking of several hydrocarbon feedstocks such as light paraffin and naphtha [18, 19]. This approach requires high energy due to the high endothermic nature of the reaction which occurs at temperature range of 700 – 900 °C according to Boyadjian *et al* [23], consuming about 30% of the overall refinery energy [22], coupled with uncontrollable product selectivity [24]. With the increasing economic consideration and the growing demand for these olefins, catalytic cracking of naphtha or heavier hydrocarbons offers a more favorable, less energy demand, and control over desired product selectivity and yield. Catalytic cracking can be carried out at lower temperature, and parameters such as

propylene/ethylene yield ratio can be controlled through β-scission mechanism [24], and coke formation can be mitigated [23].

Most commonly used catalysts for catalytic cracking are zeolites, and the use of metal oxides have also been researched and applied. Zeolites are aluminosilicates with high crystallinity, surface area, high acid strength, intracrystalline microspores, and high molecular-sieving ability to enhance shape selectivity for processes such as alkylation [22]. The use of metal oxides for hydrocarbon have also been investigated. Catalytic oxidative cracking of hexane was performed over MoO_3-Li/MgO catalyst with good activity and selectivity towards light olefins at low temperature range of 475 – 575 °C [23]. The authors reported that the cracking of hexane occurs on Li^+O^- site of the metal oxide catalyst however, the possible deactivation of the active sites when contacted with CO_2 which is a reaction product, was a challenge.

Catalytic cracking of hydrocarbons has a classical ionic mechanism which is executed either by the classical β-scission (bimolecular) of carbenium-ions chain or protolytic (monomolecular) cracking mechanism [25, 26]. For metal oxide catalysts, the surface metal ions execute the cracking process when they come in contact with the hydrocarbon feed while the bronsted acid sites are mostly responsible in zeolites. Monomolecular cracking mechanism is favored by high temperature and it involves protonation of the paraffin (hydrocarbon) to form a protonated paraffin as intermediate, by the acid sites on the catalyst involved [25]. Haag et al reported that the protonated paraffin, also referred to as penta-coordinated carbonium ion, which breaks down to form the products. The rate limiting step is the paraffin molecule interaction with the active site, and the formation of methane, ethane and ethylene as typical products [25, 26]. On the other

hand, the bimolecular cracking mechanism is favored by low temperature and involves a hydride transfer step followed by the β-scission of the carbenium-ion intermediate. Haag et al reported that for hexane cracking, the hexyl carbenium intermediate cracks rapidly than hexane with hydrogen transfer being the rate limiting step. Typical products formed are propane, propylene, butanes and isobutanes [25], [26].

1.3 Objective of the Research

One of the main reasons for catalyzing a cracking reaction is to find an economical route that requires lower cracking temperature and thus gives less energy consumption, high selectivity towards desired products. This will result in economic advantages. Ceria has the potential and possess very good catalytic activity and performance characteristics for catalytic cracking of hydrocarbons. In this research, the objective is to synthesize nano-sized ceria-zirconia (CZ) mixed oxide with a corresponding chemical composition of $Ce_xZr_{1-x}O_2$. Incorporation of iron and cobalt on CZ will be carried out with varying loading composition. These catalysts will be synthesized through hydrothermal synthesis. The obtained ceria-zirconia and doped nanocomposites will then be dried, calcined, characterized and tested for n-hexane cracking. Several characterizations will be carried out to investigate the effect of dopant incorporation on the physicochemical properties (surface area, pore size, etc) of CZ and its catalytic performance for hydrocarbon cracking. These catalysts will be tested for n-hexane cracking at different reaction conditions. Parametric variation study will be performed on the best catalyst sample which will include temperature variation and catalyst weight per feed flowrate (W/F) variation. The results

obtained will be compared, discussed and adequately reported. Regeneration of the spent catalyst will be carried out to investigate the durability, regenerative capability and the reusability of these catalysts.

In summary, the objectives will be outlined as follows:

1. Synthesis of ceria-zirconia nanocomposite.
2. Doping ceria-zirconia via incorporation of iron and cobalt to improve the characteristic properties of ceria-zirconia.
3. Characterization of ceria-zirconia and its doped nanocomposites.
4. Catalytic test of the prepared nanocomposites for n-hexane cracking
5. Parametric study on n-hexane cracking using the best catalyst nanocomposite.
6. Regeneration and reusability of the spent samples of the best performing catalyst.

CHAPTER 2

LITERATURE REVIEW

2.1 Ceria and ceria-based nanocomposites

Ceria and ceria-based oxides have widespread usage as three-way catalysts (TWCs), cracking catalyst and other catalytic applications. Ceria (CeO_2) has a framework structure similar to cubic fluorite, with 8 oxygen ions arranged at the cube edges/corners, with four cerium ions tetrahedrally surrounding each oxygen anion. Dopants improve the characteristics and catalytic performance of CeO_2, activity, thermal stability, OSC, selectivity, and so on, up to 1000°C [27]. The most commonly used dopant is zirconia (ZrO_2), as the Zr^{4+} ions are incorporated into structure lattice of CeO_2. Zirconia improves the mechanical strength of ceria, OSC as well as its redox property. CeO_2-ZrO_2 has substituted CeO_2 in various applicability of the oxide catalyst in the nineties, especially as a three-way catalyst (TWC) promoter for automobile exhaust.

The applicability of CeO_2-ZrO_2 mixed oxide catalyst is very wide owing to its high temperature stability, oxygen storage and release capacity (OSC), surface area, and stability in harsh reaction environment [3], [28]. Over time, this ceramic oxide has attracted interest in catalytic processes and it is being widely used for several catalytic activities in recent times. Being an environmentally friendly catalyst, it can be utilized for many potential industrial purposes and can be employed in reactions in which oxygen is a primary reactant at low temperature; attesting to its redox characteristic to move between 3+ and 4+ oxidation states.

Cerium ions (molecular weight of 140.116 g/mol) oxidizes easily in air and exist in two oxidation states of +3 and +4. Owing to this, ceria has the ability to undergo redox (oxidation-reduction reactions) reactions which is a major part in its ability for OSC. Ce^{4+} (tetravalent cerium) is reported to have a radius of 0.97 A° compared to Ce^{3+} (trivalent cerium) with a bigger radius of 1.14 A° and this leads to distortion of the fluorite network of ceria [29]. Ceria-zirconia oxide is an environmentally friendly oxide for cracking of heavy oil and has also seen applicability in reducing emissions from automotive exhaust, water-gas shift reactions, hydrogen manufacture, soot combustion and many other industrial activities [4], [29].

Ceria and ceria-zirconia mixed oxide can be doped with several other metals to improve their performance and physicochemical properties. Such metals can be aluminum, scandium, yttrium, neodymium, zirconia, lanthanum, and so on. Addition of these trivalent or tetravalent cations to the lattice stricture of ceria largely improves its redox ability via solid solution formation. For example, nano-sized scale incorporation of Alumina (Al_2O_3) into ceria-zirconia mixture (diffusion barrier theory) has proven to be an effective TWC for refining automobile exhaust, sustaining this catalytic performance for the car's total life span [21].

Several challenges are associated with the use of ceria and ceria composite. Synthesizing ceria composites with the optimum ratio of cerium ion to dopant ion(s) is a challenge. Chen et al reported the issue of suitable template choice with corresponding template surface adjustment to prevent homogeneous nucleation of the dopant/secondary element [30]. The authors also stressed that difficult steps and techniques are involved in the use of template synthesis for hollow ceria and composites, the dopants of noble metals

are susceptible to sintering and the recent methods are not suitable for synthesizing stable composites with noble metal nanoparticles of particle size less than 10 nm.

The research for suitable templates for large range of applicability in the synthesis of hollow ceria and its composites is still a challenge. Zhu and Mat reported ceria composite materials are unstable due to electronic conduction in fuel cell processes [31]. The prospect of using ceria and ceria composites as catalysts for cracking heavy oils via aquathermolysis in subcritical and supercritical water medium is a possibility. Ceria and ceria composites have high thermal stability and can withstand harsh reaction conditions. Although they have small surface area, these ceramics have huge prospect of replacing catalysts with larger surface areas and higher catalytic activity but low thermal stability such as alumina and zeolites.

Ce/Zr ratio and morphology of ceria are paramount to the behaviour of CeO_2-ZrO_2 oxide. Dejhosseini et al reported that ceria with cubic crystalline phase nanoparticles has better OSC and performance than octahedral nanoparticles [4]. Performance of pure ceria degrades as temperature increases due to reduction in its surface area and OSC, zirconia incorporation mitigates this degradation and enhances its OSC at elevated temperatures and also maintains the surface area via thermal sintering reduction. This enhanced OSC is evident even at low surface area of the cation-doped oxide, which is greater than that of pure ceria [6].

2.1.1 Applications of ceria-based composites

Ceria-based composites possess ranges of utility due to their unique properties, creating versatile applications of these composites in various processes and daily activities. Ceria-based composites can be used as catalysts in processes such as emission control in

volatile organic compounds (VOCs) automobiles as a TWC (Three Way Catalyst), cracking of hydrocarbons to olefins, dehydrogenation, solid oxide fuel cells and other products, and cracking of heavy oils, etc. Catalytic applications can also be found in waste water treatment, desulfurization and denitrification of SO_x and NO_x industrially, chemical processes such as oxidation and manufacture of various chemical substances. It can also be used in biomedical applications, as well as polishing agent. Ceria-based composites have also found applications as gas sensors, corrosion inhibitors, ultraviolet (UV) ray absorption, and so on [32].

2.2 Hydrothermal Synthesis of Ceria Nanocomposites

Hydrothermal synthesis of metal oxides and catalysts involves the crystal growth of the desired oxide or catalyst in the presence of high temperature and pressure. Parameters involved such as temperature, reaction time, acidity, concentration etc. can easily be manipulated to obtain desired particles sizes and morphology. In hydrothermal synthesis, the prepared precursor solution will be mixed and allowed to react in a reactor placed in a hydrothermal oven for specific duration of time and temperature. After this, the obtained product will be washed and filtered before drying and calcination. Ceria and ceria-based nanocomposites can be synthesized in a one-step method at a reduced temperature, using solvothermal/hydrothermal technique [33], [34]. Yuan et al and Tapan et al outlined regulated morphology and composition with high activity, due to high crystallinity and low agglomeration of the obtained nanocomposite. Table 2.1 gives a summary of some hydrothermal synthesis of ceria and ceria nanocomposites

Required nanocomposite shape can be obtained by hydrothermal synthesis without the need for templating agents. Parameters such as concentration, reaction time, pH,

mixture/solvent concentration and hydrothermal temperature can be varied during the process in order to obtain different shapes and sizes of ceria nanoparticles. Uniform particle size and high homogeneity can be obtained using this technique at a low temperature. Tapan et al synthesized ceria-based nanocomposites (Pt/NiCeOx, Pt/PdCeOx, Pt/FeCeOx) for direct alcohol fuel cells using a two-step synthesis. The authors prepared ceria supports by hydrothermal synthesis, followed by metal loading of the support via impregnation (incipient wetness) [35]. Stable structure of CeO_x loaded with Pt and Pd was obtained, $Pt/PdCeO_x$ showed large oxygen composition, bifunctional mechanism was observed when the CeO_x support was loaded with Pt/Pd and Fe_2O_3/Pt and PdCeOx, PtCeOx showed small particle sizes. Zhang et al prepared face-centered cubic ceria-zirconia composites via one-step hydrothermal synthesis technique. Varied ratio of ceria/zirconia ware prepared by using respective amounts of cerium and zirconium nitrates dissolved in deionized water, mixed and placed in a hydrothermal furnace using 100 mL TFE-lined autoclave, at 373 K for 10 – 48 h [36]. Face-centered cubic crystalline phases of CeO_2 were obtained. The authors reported a decrease in surface area as the calcination temperature increases from 673 K to 1173 K. Hirano and Kato also synthesized CeO_2 via hydrothermal technique using heated solution of cerium salts and urea [37]. The authors obtained cubic and octahedral sizes of ceria powder with crystallite sizes ranging from 10 – 25 nm, and reported a reduction in particle size and crystallinity as urea concentration increases. Nano-sized truncated octahedral-shaped CeO_2 was synthesized by Wang et al using cerium ammonium nitrate and ammonium hydroxide solution as precursors. Sizes ranging from 3 – 10 nm were obtained, with a mean size of approximately 6 nm [38]. CeO_2 nanorods were

Table 2.1. Hydrothermal Synthesis of Ceria and Ceria Nanocomposites

Precursors and Solvents or Surfactants	Experiment	Result	Ref
N-Hexadecyl-N,N,N-trimethyl ammonium bromide, $ZrCl_4$, $CeCl_3 \cdot 7H_2O$, NH_3, Distilled water	12g CTAB dissolved in 100 ml distilled water. Stoichiometric ratios of Ce and Zr salts in 50ml distilled water, mixing for 30 mins at 323K followed by dropwise addition of NH3. Overnight stirring at 323K followed by heating at 723K for 24h in a propylene container. Drying at room temperature and calcination at 573K for 15h	ceria-zirconia mixed oxide	[39]
$Ce(NO_3)_3.6H_2O$, $ZrO(NO_3)_2.2H_2O$, deionized water	Ce and Zr nitrates dissolved in DI water to give 0.1M cerium and 0.3 M zirconium solution, mixing, Tube reactor at 150, 180 and 200°C reaction temperatures and 5MPa. Electric furnace and heating for 18h. Drying at 60°C for 6h and calcination at 900°C for 6h	Sphere-shaped Ce/Zr oxide 35 nm, 61 nm and 31 nm respectively	[40]
$Ce(NO_3)_3.6H_2O$, $CO(NH_2)_2$, NaOH, distilled water	24mmol urea, 4mmol $Ce(NO_3)_3.6H_2O$, 80ml water. 80°C, 24h in jar to give $Ce(OH)CO_3$ nanorods. Adding 20mL distilled water and NaOH, autoclave at 120°C for 18h, 24h, 48h, 54h, 60h. Vacuum drying	CeO_2 nanotubes 50-100 nm diameter	[41]
$Bi(NO_3)_3 \cdot 5H_2O$, $(NH_4)_2Ce(NO_3)_6$, NaOH, Deionized water (DI)	Metal salts dissolved in DI water, 8M NaOH, stirring. Autoclaves in hydrothermal reactor at 220°C for 20h without stirring. Washing with DI and ethanol, vacuum drying for 24h	$Bi_xCe_{1-x}O_{2-x/2}$ Spherical, 3.5 - 5 nm diameter	[42]
$ZrO(NO_3)_2 \cdot xH_2O$, $Ce(NO_3)_3.6H_2O$, KOH, water	Microwave-Hydrothermal synthesis. 7.5mL of each salt solution, 25mL 1.2M KOH, 50mL double walled TFE. Washing with distilled water, ambient drying, calcination at 1000°C	Cubic phase $Ce_{0.75}Zr_{0.25}O_2$ 6 - 7 nm	[43]
$Ce(NO_3)_3.6H_2O$, $Na_2S.9H_2O$, distilled water	$Ce(NO_3)_3.6H_2O$ and $Na_2S.9H_2O$ in 20mL distilled water, stirring, 60mL TFE liner, 150°C for 13h in hydrothermal reactor. Drying at 60°C for 6h	Cubic CeO_2 nanorods	[33]
$Ce(SO_4)_2.4H_2O$, $Ce(NH_4)_4(SO_4)_4.2H_2O$, Urea	25 cm^3 TFE-lined autoclave, thermostat oven, constant rotation at 120 - 180°C for 5h. Washing, drying, and calcination up to 900°C	CeO_2 powders 3nm	[37]

$Zr(NO_3)_4.5H_2O$, $Ce(NO_3)_3.6H_2O$, $CO(NH_2)_2$, deionized water	70mL deionized water, 100mL TFE-lined autoclave, 373K for 10 – 48h, cooling to room temperature, repeated washing with distilled water and ethanol. Drying at 353K and calcination at 673K for 5h	Ceria-zirconia nanocomposites	[36]
$NH_4(Ce(NO_3)_6$, NaOH, deionized water	1.6g Ce salt in 5mL DI water. 6M, 35mL NaOH added, stirring for 30mins. 50wt.% transition metal salt in DI water is added. TFE-lined autoclave, 100°C for 24h. Washing and drying at 60°C for 12h	Ceria based nanocomposite 1 – 100 nm (transition metal dependent)	[35]

synthesized by Yin et al using precipitant salts of strong base-weak acid $Na_2S.9H_2O$. Face-centered cubic crystals were obtained, with 30 nm diameter and length of 300 nm [33]. The authors reiterated that pH of the mixture influences morphology of the nanorods and pure phase ceria nanorods were only obtained at pH greater than 10. $Ce_{0.75}Zr_{0.25}O_2$ were synthesized using microwave-hydrothermal synthesis by Potdar et al [43], obtaining a cubic fluorite structure with surface area of 125 m^2/g and particle size of 7 nm.

2.3 Morphology and Oxygen Storage and Release Capacity (OSC) of Ceria and Ceria Nanocomposites.

2.3.1 Size and morphology control of Ceria

The size and morphology of ceria and ceria nanocomposite can be controlled by synthesis techniques and the reaction conditions during the synthesis. Several synthesis techniques can be used in developing ceria catalyst and its composite, from the traditional/conventional methods to recent and novel approaches. The size and morphology affects the activity and performance of ceria, dictating its stability especially in severe reaction medium. Redox ability and OSC of ceria composites depends on size and morphology of the mixed oxide. Crystallinity, particle size, species concentration/content, lattice structure, shape, are all morphological properties that can be controlled by process parameters such as temperature adjustment, nucleating time, aging time, drying and calcination temperature, etc.

Properties such as surface area and OSC of ceria and ceria nanocomposites depend on the morphological structure and size of the synthesized catalyst. Temperature-dependent morphology and size control is reported in a work by Zhang et al Transmission electron micrograph (TEM) images of $Ce_{0.8}Zr_{0.2}O_{2-y}$ showed an increment in particle size as the annealing temperature increases. Size distribution of the oxide also increases correspondingly by ±35 % [44] and cubic phase crystallite sizes increase as the annealing temperature increases from 800 °C to 1250 °C. Controlling the size and morphology of ceria and ceria composites by calcination is evident in the work by Dong et al. The authors revealed an increase in crystallite size after calcination, with the fresh catalyst showing smaller sizes [3]. Also, BET surface area decreased as calcination temperature increases due to increased particle sizes.

Base concentration and temperature interplay can be used to control the shape and morphology ceria. Mai et al hydrothermally synthesized cubic ceria nanopolyhedra at very low base concentration of NaOH (0.01mol/L) and temperature between 100 – 180 °C. Cubic ceria nanorods and nanocubes can be obtained at higher base concentrations and hydrothermal temperatures of 100 °C and 140 – 180 °C respectively [20]. Another important controller of catalyst shape and morphology are crystal growth behavior, oxide synthesis as well as nanorods and nanocubes [45], [46].

Ionic surfactants can be used to influence size, shape, morphology control and particle cluster according to Gnanam and Rajendra, via hydrothermal synthesis. Surfactant incorporation with precursors lead to better crystallinity and enhanced crystallite growth, giving a cubic fluorite structure. Stretched spherical-like particles with small particle size were obtained with anionic surfactant incorporation, flower-petal-shaped morphology was

obtained with non-ionic surfactant while small, clustered rod-like CeO_2 nanoparticles with cationic surfactant [47]. Mean crystallite sizes of 12.53 nm, 13.24 nm and 16.07 nm were obtained respectively. Cui et al synthesized cerium carbonate hydroxide and CeO_2 micro and nanostructure via surfactant-assisted hydrothermal technique. Synthesis time, urea concentration and temperature variations controlled the particle size and morphology of the synthesized structures [48]. Hydrothermal synthesis of ceria nanocrystal in the presence of methanol, for CO_2 conversion was performed by Wang et al Nanorods, spindle-like, octahedron and nanocube morphologies were obtained, with correlation to product yield, BET surface area, pore volume and average pore size [49]. Effect of precipitant and aging temperature on morphology control was studied by Minamidate et al Pre-aging at low temperature of 25°C resulted in monodispersed spherical precursor while rod-like nanoparticles were obtained at 50 °C, for 72 hours [50]. The authors also revealed that crystalline-structured powders were obtained without aging while an amorphous-like structure was obtained for powders with aging treatment preparation. Cubic phase was obtained after calcination at 400 °C in all cases.

The morphology of ceria and ceria composite is such that the crystal lattice allows mobility of oxygen ions in the lattice network. This is a major factor in the redox ability of cerium ions with +3 and +4 oxidation states and OSC of ceria and ceria nanocomposites. Longer aging time influences the morphology and textural properties of ceria-zirconia mixed, as well as increase in surface area of the mixed oxide [51]. Kim et al investigated the effect of aging time and synthesis technique on the morphology of ceria-zirconia nanocomposite. Supercritical synthesis of the mixed oxide gave larger BET surface area and pore volume than precipitation technique, but lesser total oxygen storage and release

capacity [52]. Also, better thermal stability and sparsely arranged morphology was observed in oxides via supercritical synthesis while precipitation technique gave densely agglomerated morphology. The authors also discovered that BET surface area, pore volume and total OSC were reduced after aging while crystallite size increased with precipitation method.

2.3.2 Oxygen storage and release capacity (OSC)

Oxygen storage and release capability (OSC) is the ability of a catalyst to capture and as well release oxygen molecules via its surface area during an oxidation-reduction cycle. It is one of the main importance of ceria (Cerium IV dioxide, CeO_2) nanocatalyst as a three-way catalyst (TWC) in engine exhaust and for the cracking of heavy oils. Over the years, OSC measurements are commonly carried out with techniques such as, temperature programmed reduction (TPR), the use of x-ray diffraction (XRD, typically for structural examination of ceria) and in some cases, density functional theoretical (DFT) evaluations are carried out.

OSC of ceria has gained recognition in the literature works by many researchers in recent years. It was discovered that the oxygen molecules are attached to the oxygen vacant sites that are present on available catalyst surface area thus; there is a relationship between the OSC of a catalyst and the available surface area of such catalyst. Several factors govern the OSC of a ceria composite catalyst such as calcination of the catalyst, shape (which deals with the stoichiometric and the oxygen vacant sites), size of the catalyst (usually in nanometers), doping (addition of transition metal oxides to the catalyst to increase its stability and reduction capability) and morphology and characterization of the ceria structure, which can be determined using XRD, or TEM (Thermal Emission Microscopy).

The stability of ceria and ceria-based composite nanoparticles is of paramount concern. Cerium has two stable oxidation states of +3 and +4 and their oxides are Ce_2O_3 and CeO_2 respectively. These two stable oxidation states account for the strong red-ox (reduction-oxidation) capability of ceria which gives it the capability to store and discharge oxygen molecules, which is being measured through the OSC of ceria [53]. Thus, cerium ions can move from Ce^{3+} to Ce^{4+} during oxidation and vice versa during reduction. Air to Fuel ratio fluctuations in car exhaust can be reduced by using Ceria as a sub-catalyst, to stabilize the partial pressure attributed to the oxygen gas [5].

Doping ceria nanoparticles with oxides of metals (e.g transition metals) increases its efficiency and performance. Ceria is commonly doped with metallic oxides such as zirconia (ZrO_2), alumina (Al_2O_3). Oxides of titanium, tin, manganese and etc, can also be used. Basically, these dopant ions have different stable oxidation states thus, they can exhibit red-ox reaction cycle [7], therefore increasing the oxygen storage and release capability when doped with ceria particles. Shen et al reported that at a frequency of 0.1Hz and 0.05Hz and temperature of 450 ^oC, $Ce_{0.67}Zr_{0.33}O_2$ has a better dynamic OSC than CeO_2 which is evident from the larger peak of the CO_2 curves for $Ce_{0.67}Zr_{0.33}O_2$ compared to CeO_2, in the plot of concentration (%) against time [54]. The increase in OSC as a result of doping ceria nanoparticles can be attributed to the fact that these dopants increase the movement of oxygen molecules on the available surface area.

2.4 Acidity/Basicity and OSC Properties of Ceria-Based Catalysts and their Roles in Upgrading of Heavy Hydrocarbons and Oils.

Ceria is known to be an amphoteric oxide, having both properties of an acid and a base which could be improved through the incorporation of suitable dopant ions such as

zirconium [55]. Some of the many merits of ceria-based catalysts are the ability to exhibit redox properties, oxygen storage and release capacity, and acid-base characteristics. These properties are interrelated and they have different roles in cracking heavy hydrocarbons and oils. Availability of acid and basic sites on the surface structure of cracking catalysts is paramount for evaluating their properties and activity[56]. Catalysts such as zeolites are known to possess Bronsted and Lewis acid sites which aid their catalytic performance for specific reactions such as oxidation, dehydrogenation, cracking of heavy hydrocarbons, etc.

The acidity/basicity of ceria based catalysts can be measured using Hammett acidity function H_o. Doping ceria influences the strength of the surface Lewis acidity or Lewis basicity of the catalyst, depending on the type and properties of the dopant. Zirconia is commonly used for doping ceria and it possesses appreciable amount of acidic and basic sites as reported by Stošić et al [56]. According to the work of Vivian and Duprez, ceria has remarkably lower Lewis acidity compared to zirconia, and this decreases when ceria is being reduced [57]. The authors also reported a higher basic site density (3.23 $mmolCO_2m^{-2}$) than zirconia (1.77 $mmolCO_2m^{-2}$). This indication points to the fact that the basic sites of ceria have weak or medium strength while that of zirconia is very strong even with lower density.

Experimentally, acidity and basicity of ceria based catalysts are determined by NH_3 and CO_2 adsorption respectively, using microcalorimetric method or temperature programmed desorption (TPD). Hammett indicators can also be used by monitoring the color changes of the indicator to respective conjugates. Ge et al investigated the effect of doping γ-Al_2O_3 with CeO_2 and found out that, the incorporation of ceria into γ-Al_2O_3

increases the basicity of the catalyst while an adverse effect of acidity reduction was observed [58]. The authors also found no deposition of coke during the dehydration reaction in carbon dioxide over the catalyst. This can be attributed to the redox ability Ce^{4+}/Ce^{3+} of ceria to produce free and active oxygen atoms through the activation of CO_2 on basic sites of the catalyst via surface basicity. This correlates with the affirmation by Dejhosseini et al that in-situ production of oxygen and hydrogen species prevents coking during the upgrading of heavy oil in SCW. Thus, the OSC of ceria and ceria based catalysts will aid in-situ supply of oxygen species for needed oxidation and their redox capacity will enhance the generation of hydrogen atoms which limits coke formation. This is highly needed in upgrading heavy oils especially in SCW, which is a radical source as well as highly oxidative and less favorable reaction medium for catalysts. Also, the limiting of coke formation which is a solution to the major challenge in heavy oil upgrading. Solid acids of ceria and ceria-based catalysts were synthesized by Vankatesh et al and pure ceria was found to have the lowest total surface acidity while SO_4^{2-}/Ce-Zr oxide has the highest [55]. The total surface acidity and yield of quinoxaline were proportional and the selectivity of the products formed was also dependent on the strength of the acid sites [55]. An observation was noticed as the authors reported that by-products were produced due to the strong acid sites of the sulphated Ce/Zr oxide thus, having less selectivity towards the formation of desired product. Petallidou et al investigated the effect of Lanthanum ions on acidity of ceria and found out that doping ceria with up to 20% La increases the surface acidity of acid sites of $Ce_{1-x}La_xO_{2-\delta}$ oxide [59]. According to the authors, further increment in La composition in the mixed oxide reduces the concentration of the acid sites. Also, they found a relationship between surface area of the catalyst oxide and its surface acidity,

reporting a direct proportional correlation between the concentration of the acid sites and the surface area. Sugunan and Seena observed that surface oxygen ions of the crystal lattice structure of ceria donates electron but the donating capacity decreases as temperature decreases [60]. The reduction is due to the decrease in surface hydroxyl ions and limited mobility as the temperature increases. Electron donation is an intrinsic acidic property and this is also facilitated by OSC properties of ceria. Strong acid sites of ceria supported of sulphated zirconia was improved with little amount of potassium addition although, there was a drop in the total surface acidity of the catalyst [61]. This was computationally investigated by Wang et al using density functional theory.

2.5 Redox Properties of Ceria Nanocomposites.

Ability of ceria to move between oxidation states of +3 and +4 highlights one of its unique properties. Redox property of ceria is an important characteristic that outlines its ability for OSC, thus it can undergo reduction as well as oxidation in needed reactions. The study of intrinsic reduction property of ceria based catalyst is paramount. This can be done using Temperature Programmed Reduction (TPR) technique. The redox property has a relationship with the OSC of ceria based nanocomposites because it involves reduction and oxidation, evident with the variable oxidation state of ceria. Also, the redox characteristics of ceria-based nanocomposites can be related to acidity and basicity of these mixed oxides. Damyanova et al performed TPR on ceria-zirconia oxides after calcination [62]. The authors reported that reduction of Ce^{4+} to Ce^{3+} initiates at the surface before extending to the bulk area of the oxide. Also, hydrogen consumption by these ceria-zirconia oxides were highest for samples calcined at 1073 K than those calcined at 773 K although, the peak

temperature recorded was random rather than chronological with the temperature and concentration increment [62].

However, the higher the temperature, the higher the chances of ceria-based oxides losing their intrinsic properties. Aneggi et al attested to this in their work [63] where they reported the reduction behavior ceria-based oxides under H_2-TPR and rapid redox conditions. They stated a step-wise model in which surface reduction of the Ce^{4+} occurs before bulk reduction of the Ce^{4+} layers which occurs at higher temperatures [63]. The first step is the surface reduction which is responsible for the creation of oxygen vacant sites while the second step (bulk reduction) is responsible for the extension of these sites into the bulk of ceria-zirconia mixed oxide [29]. Doping ceria with zirconium ions improves the basic properties of ceria as well as its redox property. TPR measurement involving total H_2 consumption can be interpreted and used as measurement of total OSC for ceria-based oxides such as ceria-zirconia oxide [63]. Alessandri et al reported the presence of two peaks after redox activities performed on $Ce_2Zr_2O_8$ [64], each one representing high and low temperature accordingly. The authors also reported modifications in the surface configuration of cations in the ceria nanocomposite but this information is limited as regard the comprehension of low temperature reduction of the composite. However, the presence of these two peaks explains the active presence of both small and large ceria crystals in the high TPR process [29].

2.6 Effect of Synthesis Parameters on Ceria Nanocomposites.

There is interconnectivity between the morphology of ceria based nanocomposites and the synthesis parameters involved during the synthesis process. Parameters such as temperature, synthesis time, composition of cerium and other cations or dopant ions, aging,

etc. has effect on the shape, size, stability, and morphology (lattice structure, crystallite size, etc.) of the nanocomposites. These parameters can be varied and optimized to obtain the desired catalyst nanocomposite which also depends on the process requirement in which the nanocomposite is needed. Adequate interplay between these parameters and necessary adjustments can be very vital to catalytic performance of ceria-based nanocomposites.

2.6.1 Effect of composition.

Ce and Zr composition in the mixed oxide nanocomposite is very paramount. Percentage composition of each chemical element have morphological effect on the lattice structure and phase of the as-synthesized catalyst. Adding zirconium to ceria improves its intrinsic properties such as stability, surface area, thermal stability, OSC, redox properties, and so on. According to Pudukudy and Yaakob, different molar ratio of cerium and zirconium can lead to different phases of ceria-zirconia solid solution [29]. Ceria possesses low surface area but doping it with zirconium increases the surface area. As the zirconium content in ceria-zirconia nanocomposite increases, the BET surface area reduces while the mean crystallite size increase [65], [66]. Liang et al employed the use of template with ultrahigh surface area carbon material to obtain BET surface areas greater than 100 m^2/g as the zirconium content varies correspondingly. On the other hand, BET surface areas of ceria-zirconia nanocompoiste obtained by Gnanam et al were below 50 m^2/g, decreasing as the Zr content increases and this typifies the low surface area of ceria-zirconia nanocomposites, according to literature.

Doping ceria with zirconium enhances the stability (mechanical and thermal), OSC, redox properties and other intrinsic properties of ceria. According to literature, zirconium

content between 15 – 25 % are best suitable for doping ceria [47], [65], [66]. Increased acidity of ceria-zirconia mixed oxides increases as zirconium ion content increases but OSC and redox property of the mixed oxide increases as cerium content increases. Also, incorporation of zirconium into ceria enhances oxygen movement in the crystal lattice as a result of lattice defect in the mixed oxide lattice structure [29]. Thermal resistance of ceria-zirconia nanocomposites reduces as Ce/Zr ratio increases, indicating an inverse relationship between thermal resistance and zirconium content in the nanocomposite. Composition effect was also investigated on prepared samples of pure ceria, ceria-lanthana and ceria-zirconia for oxidation of soot at low temperature by Katta et al The authors discovered that ceria-lanthana possess higher lattice deformity and oxygen vacant sites due to greater redox property than ceria-zirconia and pure ceria [67]. Thus, oxidation of soot was increased probably due to the presence of more available active oxygen atoms due to the doping effect of Lanthanum ions. Also, lanthanum-doped ceria possess higher OSC and thermal stability than zirconium-doped ceria [67].

2.6.2 Effect of Temperature.

Temperature effect in the synthesis of ceria-based nanocomposites can be studied based on synthesis temperature and calcination temperature approach. Synthesis temperature in the preparation of ceria-based nanocomposites have huge influence in particle and crystallite size, morphology and other associated properties. Yin et al synthesized ceria nanorods and found out that, as the synthesis temperature increases from 75 ^{o}C to 225 ^{o}C, the morphology of the as-synthesized ceria gradually changes from nanorod to spherical crystalline nanoparticles [33]. Ceria-zirconia mixed oxide was also synthesized by Machmudah et al at temperatures ranging between 150 – 200 ^{o}C in a batch

reactor for 18 h [40]. The authors discovered higher XRD peak intensities at 180 ^{o}C and 200 ^{o}C while lower peaks were observed at 150 ^{o}C while SEM image obtained at 180 ^{o}C was blurred.

According to literatures, the possibility of losing surface area of ceria-zirconia nanocomposite at high calcination temperatures cannot be neglected. Kaspar et al attested to this fact and the authors reported that loss of surface area was due to phase segregation during calcination [68]. Thammachart et al reported the influence of calcination temperatures on the morphology and surface area of ceria-zirconia catalysts. The authors discovered high BET surface area of more than 100 m^2/g at 500 ^{o}C while at 900 ^{o}C, the surface area was extremely low with about 100 m^2/g lower than that of 500 ^{o}C for various zirconia content at both reflux times of 50 h and 120 h [69]. A contrasting report was seen in the work of Sohn et al regarding the surface area and calcination temperature. The authors reported higher surface area of sulfated ceria-zirconia catalyst at high calcination temperatures and low surface area at low calcination temperature [70]. Reaction temperature and calcination temperature are thus paramount to the final morphology and properties of ceria-based nanocomposites.

2.6.3 Synthesis and aging time effect.

Controlling the aging and synthesis time is very important in catalyst synthesis. Ceria-based nanocomposite are well known to be influenced by temperature nonetheless, the time duration at which the synthesis is being performed is very important. Synthesis duration influences the size, shape and morphology of ceria-based nanocomposites, and thus, invariably affecting their catalytic performances. Liotta et al prepared ceria-zirconia at varying time of 1 day, 1, 2 and 3 weeks respectively. The authors discovered similar

XRD patterns after calcining the samples at 923 K but their BET surface increases proportionally with the synthesis time respectively [51]. Also, mesopore volume, total porosity and mesopore surface area increase accordingly with synthesis duration while mesopore size distribution, bulk and skeletal density and particle diameter decrease with time.

In the already cited work of Yin et al, the authors investigated the effect of synthesis time at 150 ^{o}C and discovered morphological changes, as well as varied size and shapes of the synthesized ceria, and this is evident in the SEM images [33]. Thus, the longer the synthesis time, the higher the crystallinity of ceria-based nanocomposites. Aging time also have effect on the morphology of ceria-based nanocomposites. Minamidate et al synthesized spherical and rod-like ceria particles by varying the pre-aging duration in the precipitation synthesis process [50]. Rod-like shapes were obtained at 24 - 50 h pre-aging time while monodispersed spherical orientation was obtained at pre-aging time of 72 – 120 h. The authors also found that amorphous carbonate of ceria was obtained when the synthesis was carried out without pre-aging. Thus, it is imperative to take cognizance of synthesis duration and aging time effect where applicable. This affects the morphology and can thus, affect properties such as OSC which rely on the lattice structure and oxygen vacancies and mobility in the structure.

2.6.4 Effect of surfactants.

Catalyst synthesis involves practical and technical approach in the preparation process to obtain desired morphology, size, shape and few controllable properties. This can be achieved with the introduction of surfactants and precipitants. The morphology of ceria-based nanocomposites can be dictated by the type and influence of surfactant used in the

synthesis process. Adding surfactants to precursor solutions in the synthesis of ceria-based composites can improve crystallinity. Surfactant addition also influences the size, shape and lattice structure of ceria nanocomposites. Gnanam et al used polyethylene glycol (PEG), cethyltimethyl ammonium bromide (CTAB), and sodium dodecyl sulfate (SDS) surfactants to prepare CeO_2. PEG gave CeO_2 with flower-type shapes, SDS gave small size particles with spherical morphology with elongated shapes and CTAB gave small, rod-shaped particle clusters [47]. Also, the authors reported a strong adsorption of the as-synthesized ceria in the ultraviolet (UV) region, owing to the effect of surfactants in the hydrothermal synthesis procedure. Yin et al used $Na_2S.\ 9H_2O$ as precipitant for synthesizing ceria nanorods. The precipitant acted as a strong base-weak acid, making the reaction process controllable to desired effect [33]. Thus, morphological controlled of ceria based composites can be achieved via the use of suitable surfactants and precipitants as this can improve the catalytic properties of the catalysts.

CHAPTER 3

EXPERIMENTAL

3.1 Materials

All chemicals used were of analytical grade. Cerium III acetate (Sigma-aldrich, 99.9 %), Zirconium oxynitrate (Sigma-aldrich, 99 %), potassium hydroxide (86 %), Cobalt VI chloride hexahydrate (BDH Chemicals, 99 %), Iron III nitrate nonahydrate (PRS Pancreac, 98 %), ethanol (Sigma Aldrich, 99%), n-hexane (Sigma-aldrich, 97%).

3.2 Experimental Procedure

List of the samples to be prepared are outlined with details as follows:

CZ: ceria-zirconia nanocomposite (25% Zr and 75% Ce).

CoCZ: cobalt-doped ceria-zirconia nanocomposite (20% Co, 20% Zr and 60% Ce).

FeCZ: iron-doped ceria-zirconia nanocomposite (20% Fe, 20% Zr and 60% Ce).

FeCoCZ_A: Iron, cobalt co-doped ceria-zirconia nanocomposite (10% Fe, 10% Co, 20% Zr and 60% Ce).

FeCoCZ_B: Iron, cobalt co-doped ceria-zirconia nanocomposite (5% Fe, 5% Co, 20% Zr and 70% Ce).

3.2.1 Pure ceria-zirconia nanocomposite (CZ).

Ceria-zirconia, $Ce_{0.75}Zr_{0.25}O_2$ (CZ) was prepared using hydrothermal synthesis technique and template-hydrothermal synthesis technique. The solution was prepared by dissolving 4.7368 g of cerium III acetate ($Ce(CH_3CO_2)_3.H_2O$) and 1.5789 g of zirconium oxynitrate ($ZrO(NO_3)_2.H_2O$) in 53.1579 g of deionized (DI) water followed by magnetic

stirring at 500 rpm at room temperature for 1 h. Simultaneously, 0.5263 g of KOH was dissolved in 10 g of DI water followed by magnetic stirring at 300 rpm for 1 hr. After stirring the precursor salt solution for 1 h time, KOH solution was slowly added to the salt solution using a dropper while stirring continues for another 3 h at room temperature for total dissolution of the salt precursors in the deionized water. This will enhance aging and nucleation. The resulting solution was transferred to 100 mL TFE-lined steel autoclave which was tightly bolted and clamped to the holding shafts for rotation at 40 rpm in the hydrothermal oven. The oven was set at a temperature of 180 ^{o}C for 24 h. Air drying for 18 h was carried out followed by drying in air (fume hood) at 75 ^{o}C and then calcined at 600 ^{o}C for 6 h.

3.2.2 Iron-doped ceria-zirconia nanocomposite (FeCZ).

Fe-doped ceria-zirconia, FeCZ ($Fe_{0.2}Ce_{0.6}Zr_{0.2}O_2$) was prepared via hydrothermal technique by dissolving 1.145 g of $Fe(NO_3)_3.9H_20$, 3.435 g of $Ce(CH_3CO_2)_3.H_2O$ and 1.145 g of $ZrO(NO_3)_2.H_2O$ in 58.7 g of deionized water and stirred at 500 rpm for 1 h at room temperature. Simultaneously and separately, 0.573 g of KOH was dissolved in 10 g of deionized water and stirred at 300 rpm for 30 min. After stirring the precursor salt solution for 1 h, KOH solution was slowly added to the salt solution using a dropper while stirring continuously for another 3 h at room temperature for total dissolution of the salt precursors and aging. The resulting solution was transferred to a 100 mL TFE-lined steel autoclave and placed in a hydrothermal reactor unit at 180^{o}C for 24 h. The prepared sample was collected and washed with deionized water via centrifuging. The collected sample was dispersed in ethanol, transferred to a crucible and dried in air for 24 h. This is followed by drying at 75 ^{o}C in air for 6 h and then calcined at 600 ^{o}C for 6 h.

3.2.3 Cobalt-doped ceria-zirconia nanocomposite (CoCZ).

The same procedure as in 3.2.2 was used but the Fe component was replaced with $CoCl_2.6H_2O$ to obtain cobalt-doped ceria-zirconia ($Co_{0.2}Ce_{0.6}Zr_{0.2}O_2$) using the same weight measurements and synthesis order.

3.2.4 Cobalt, Iron co-doped ceria-zirconia nanocomposite (FeCoCZ).

Co-Fe co-doped ceria-zirconia sample A ($Fe_{0.1}Co_{0.1}Ce_{0.6}Zr_{0.2}O_2$) was prepared via hydrothermal technique by dissolving 0.5723 g each of both $Fe(NO_3)_3.9H_20$ and $CoCl_2.6H_2O$, 3.435 g of $Ce(CH_3CO_2)_3.H_2O$ and 1.145 g of $ZrO(NO_3)_2.H_2O$ in 58.7 g of deionized water and stirred at 500 rpm for 1 h at room temperature. Simultaneously and separately, 0.573 g of KOH was dissolved in 10 g of deionized water and stirred at 300 rpm for 40 mins. After stirring the precursor salt solution for 1 h, KOH solution was slowly added to the salt solution using a dropper while stirring continuously for another 3 h at room temperature for total dissolution of the salt precursors and aging. The resulting solution was poured into a TFE-lined steel autoclave (100 mL) and transferred to a hydrothermal reactor oven unit at 180^oC for 24 h. Sample B ($Fe_{0.05}Co_{0.05}Ce_{0.7}Zr_{0.2}O_2$) was prepared with the same approach to sample A except for changes in weight of the precursor salts (Ce: 4.00g, Zr: 1.145 g, Fe and Co: 0.286 g) while other measurements remain the same. The prepared samples were collected and washed with deionized water via centrifuging. The obtained samples A and B were collected and washed with deionized water via centrifuging. The collected samples were dispersed in ethanol, transferred to a crucible and dried in air for 24 h. This is followed by drying at 75 ^oC in air for 6 h and then calcined at 600 ^oC for 6 h.

3.2.5 Effect of synthesis time variation on FeCoCZ_B.

Synthesis time variation was carried out on FeCoCZ_B according to time variations of 8 h, 16 h, and 24 h in the oven. This performed to observe the effect of synthesis time on crystallinity of the nanoparticles formed during hydrothermal synthesis.

3.3 Sample Characterization.

3.3.1 X-ray diffraction (XRD).

After drying the prepared samples, XRD characterization was performed in order to determine the crystallinity of the powdered nanocomposites and their phases. This was also performed after calcination in order to determine the crystallite size changes before and after calcination. A Rigaku Miniflex II Desktop X-ray diffractometer at Imaging Laboratory CENT (Center for Excellence in Nanotechnology, KFUPM) was used for this analysis. Using a start angle of 3 ^{o} and stop angle of 80 ^{o}, sampling step size of 0.03, scan speed of 3.00, 30 kV and 15 mA, the powdered samples were analyzed.

3.3.2 Field emission scanning electron microscopy (FE-SEM).

Imaging analysis of the prepared samples were performed using scanning electron microscope (Oxford Instrument, X-Max) to view the shapes and crystalline appearance of the samples in nanoscale magnification. Images were taken at SEM magnification of 200 kx with SEM high voltage of 20 kV at a scaling of 200 nm.

3.3.3 Raman spectroscopy.

Raman spectroscopy was performed to determine the extra peaks as a further analysis to XRD and also to see the effect of dopant (cobalt and iron) ions in the crystal lattice of ceria-zirconia on the Raman peaks of this catalyst. The Raman spectrometry was

carried out using Yvon Jobin Horiba Raman spectrometer (iHR320) with CCD detector with green type laser source at 532 nm, grating position of 600, exposure time of 15 s, spectrum window of 30 to 2000 cm^{-1}, laser intensity of 50 % and accumulation number of 3.

3.3.4 Surface and physicochemical analysis.

Morphological properties such as BET surface area, pore volume and pore size distribution was carried out via Micromeritics ASAP 2020 Surface Area and Porosity Analyzer (CENT, KFUPM). This was achieved using N_2-adsorption method for a downtime of 24 h at a temperature of 180 °C using 0.2 g of each sample at a time.

3.3.5 Temperature Programmed Desorption (TPD).

NH_3–TPD and CO_2-TPD were performed to investigate and evaluate the presence and strength of acid and basic sites on the prepared samples of ceria-zirconia nanocomposites. These were carried out using Chemisorb 2750 Micrometrics Chemisorption Analyzer. For both NH_3 and CO_2 TPD analysis, 0.15g of each sample were used for the experimental characterization. These samples were heated to 600 $^{\circ}$C at a rate of 30 °C/min for initial treatment, under constant flow of Helium gas at a flow rate of 25 mL/min for 30 mins. Subsequently, the samples were cooled to 45 °C and 100 °C for adsorption of CO_2 (99.9%) and NH_3 (10 %) respectively, each at 28 mL/min. The adsorption was carried out for 30 mins, followed by injection of helium gas for 1 h to flush the physisorbed gases from the surface of the sample specimens. Afterwards, the setup was heated to 900 °C at a rate of 10 °C/min for both CO_2-TPD and NH_3-TPD respectively. The quantity of desorbed gases was measured and recorded using a TCD detector at 0.5 s interval for all cases.

3.3.6 Fourier transform infrared radiation (FT-IR)

Functional group identification was performed on the ceria-zirconia and the doped nanocomposites via Thermo Scientific Nicolet 6700 spectrometer. Thin Translucent pellet were prepared by mixing known weight of each samples and KBr. Spectra reading was obtained at a scanning range of 200 – 4000 cm^{-1}.

3.3.7 Pyridine-Adsorbed Fourier transform infrared radiation (FT-IR)

Presence and type of acid site present on the prepared ceria-zirconia nanocomposites were evaluated via pyridine adsorption on the sample surface using Thermo Scientific CLASS 1 LASER PRODUCT setup connected to High Specac High Pressure/Temperature Cell Controller. The powdered samples were pelletized to thin pellets of 1.3 cm and average weight of 90 mg. The pellets were placed in the FT-IR cell and background data were taken at 25 °C. This was followed by heating to 550 °C for 30 mins for pre-treatment and further degassed to 150 °C in vacuum by cooling. Afterwards, pyridine was adsorbed on the pellet surface for 20 mins at 150 °C in vacuum, followed by desorption of pyridine for 15 mins. The spectra for respective CZ nanocomposite samples were obtained at 150 °C and outgassing temperature of 250 °C.

3.3.8 Thermogravimetric Analysis (TGA)

Weight loss of the prepared samples in different temperature regions were carried out to investigate the formation of ceria-zirconia solid solutions and their thermal stability. This was done using a Netzsch STA 449F3 at a temperature range of 30 – 1000 °C at a gas flow of 20 mL/min and heating rate of 15 °C/min.

3.4 Catalytic Testing.

CZ and its doped nanocomposites were tested for hydrocarbon cracking using Allen-Bradley PanelView Plus 600 fixed bed reactor and analysis of the cracked products were carried out using Agilent Technologies 7890A Gas Chromatography (GC) System connected online to the reactor. Hexane was used as the hydrocarbon feed. The catalytic cracking was carried out in this fixed-bed reactor column under atmospheric pressure conditions. The cracking was carried out at a temperature range of 600 – 650 °C in the presence of a carrier gas flow (N_2), and without the addition of steam. 0.3 g of each catalyst sample was weighed, pelletized, crushed and sieved to particle size of 100 – 300 nm mesh. After that, the samples were placed in the reactor column and supported with quartz wool on both end to make a catalyst bed in a reactor column of 7.92 mm inner diameter and 300 mm length. This is followed by pretreatment of the catalysts in N_2 flow at 20mL/min at 650 °C for 90 min. A type K chromel-alumel thermocouple was placed inside the column to detect and measure reaction temperature while another thermocouple was placed outside, making external contact with the reactor column in the constant temperature region of the reactor furnace.

Catalytic reactions were carried out by injecting feed using a HPLC pump (LabAlliance, Series II), at temperature range of 600 - 650 °C, 10 h time-on-stream (TOS), 20 mL/min nitrogen gas flow, catalyst weight per feed flowrate (W/F) of 0.065 h – 0.131 h and total pressure of 0.3 bar. The hexane feed was vaporized and transported by the carrier gas (N_2) to make contact with the catalyst bed to be cracked. The gaseous product analysis was done by an on-line connected gas chromatograph (Agilent Technologies,

7890A) with back and front FID detectors. The products were injected into the GC every 1 h for a period of 10 h TOS.

Carbon balance was used to calculate hexane conversions and product selectivity (i.e. carbon mole amounts in product per total number of carbon moles in overall product mixture without unconverted feed) according to the equations below.

$$\text{Hexane Conversion} = \left(\frac{C_{6,in} - C_{6,out}}{C_{6,in}}\right) X\ 100\% \quad (1)$$

$$\text{Product Selectivity} = \left(\frac{n_i C_i}{\sum n_i C_i}\right)\ X\ 100\% \quad (2)$$

$$\text{Yield} = \text{Conversion x Selectivity} \quad (3)$$

3.5 Catalyst Regeneration.

In this work, we will regenerate the best performing catalyst and CZ (base) after hexane cracking. The spent catalysts will be characterized to see the effect of coking on the surface morphology and structure of the catalyst, and effect of dopant ions on carbon deposition. The spent samples will be spread into the crucible and placed in the oven at 600 °C for 4 h to thermally regenerate the catalyst samples. After the regenerated catalysts have been characterized, it will be reused and the results are compared with that of the fresh and spent samples.

CHAPTER 4

RESULTS and DISCUSSION

4.1 X-ray Diffraction Analysis.

XRD analysis was performed for the prepared catalysts before and after calcination in order to investigate the effect of calcination on the crystalline properties and phase structure of the CZ nanocomposites. The obtained diffraction peaks were indexed to (111), (200), (220), (311), (222), (400) and (331) as shown in Figure 4.1 and Figure 4.2, before and after calcination respectively.

The miller indices obtained indicate a cubic fluorite structure with a space group of *Fm3m* as analyzed by the diffractometer. Comparatively, similar XRD patterns were obtained for CZ and the doped CZ nanocomposites (CoCZ, FeCZ, FeCoCZ_A and FeCoCZ_B), with the absence of extra peaks which confirms the formation of ceria-zirconia solid solutions with no extra phase formation. Also, the absence of extra diffraction peaks indicates full incorporation of Fe and Co ions (dopants) into the crystal lattice structure of ceria-zirconia. No extra peaks of Co and Fe oxides was observed, with no change to the basic phase structure of ceria-zirconia after doping, as observed by Wang et al and Wang et al [71, 72]. With the obtained analysis, the probable inference is that Zr^{4+}, Co^{2+} and Fe^{3+} replaces Ce^{4+} ions in the crystal lattice of ceria as a result of solubility of these dopant ions which influences the possible co-doping of these metal ions with one another, thereby allowing incorporation into the crystal lattice structure of ceria-zirconia nanocomposites in the formation of solid solutions.

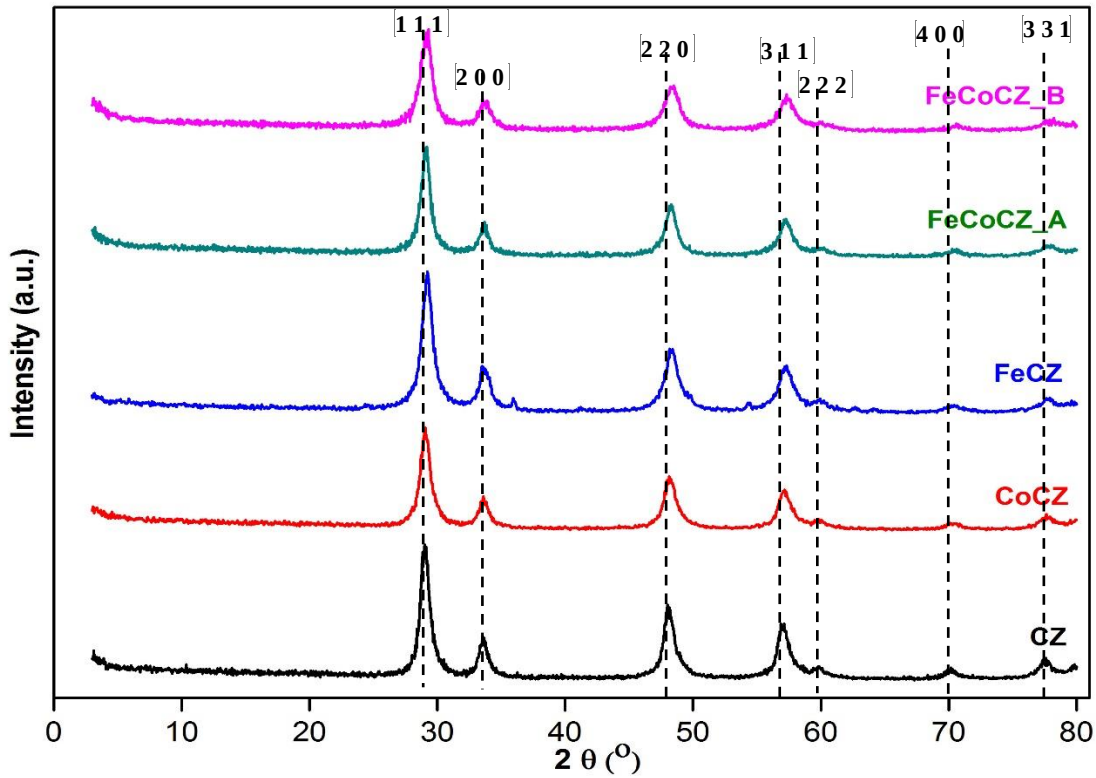

Figure 4.1 XRD peaks for CZ, CoCZ, FeCZ, FeCoCZ_A and FeCoCZ_B before calcination.

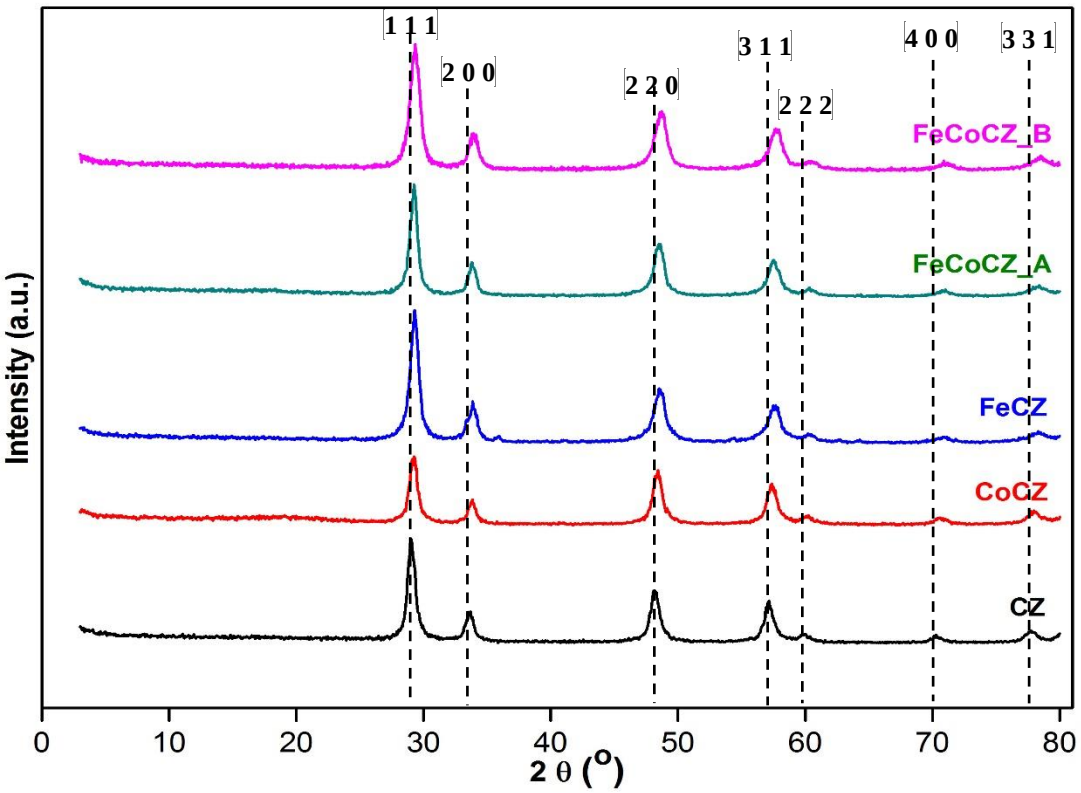

Figure 4.2. XRD peaks for CZ, CoCZ, FeCZ, FeCoCZ_A and FeCoCZ_B after calcination.

Table 4.1. Peak angles, Lattice Parameter and Crystallite size of CZ, CoCZ, FeCZ, FeCoCZ_A and FeCoCZ_B.

Sample	2 Ɵ (deg)		Lattice Parameter (Å)		Crystallite Size (nm)	
	Before calcination	After calcination	Before calcination	After calcination	Before calcination	After calcination
CZ	28.98	28.99	5.33	5.33	9.62	11.79
CoCZ	29.10	29.23	5.31	5.29	9.24	11.55
FeCZ	29.17	29.28	5.29	5.28	8.76	11.12
FeCoCZ_A	29.14	29.25	5.30	5.28	10.45	12.13
FeCoCZ_B	29.19	29.34	5.29	5.27	7.59	9.34

The obtained XRD patterns and diffraction data show slight shift in the diffraction peak positions of CoCZ, FeCZ, FeCoCZ_A and FeCoCZ_B when compared to CZ. Notable shift to slightly higher diffraction angles 2Θ, confirms the presence of Fe^{3+} and Co^{2+} incorporation and the effect of calcination temperature. Wider peaks were observed in the diffraction peaks of CoCZ, FeCZ, FeCoCZ_A and FeCoCZ_B and reduced estimated lattice parameters before and after calcination, when compared to CZ.

Synthesis time effect was investigated on FeCoCZ_B for 8, 16 and 24 h respectively. The XRD patterns shown in Figure 4.3 indicate an increment in peak intensity as the synthesis time increases. Thus, the crystallinity of the nanocomposites increases with synthesis time. Crystallite sizes of 5.43 and 6.6 nm were obtained for 8 h and 16 h synthesis time respectively. This is because of larger FWHM obtained in both cases as compared to 24 h synthesis time. However, smaller crystallites sizes were estimated for 8 and 16 h synthesis time, the XRD peaks shows that better crystallinity was obtained at 24 h synthesis time.

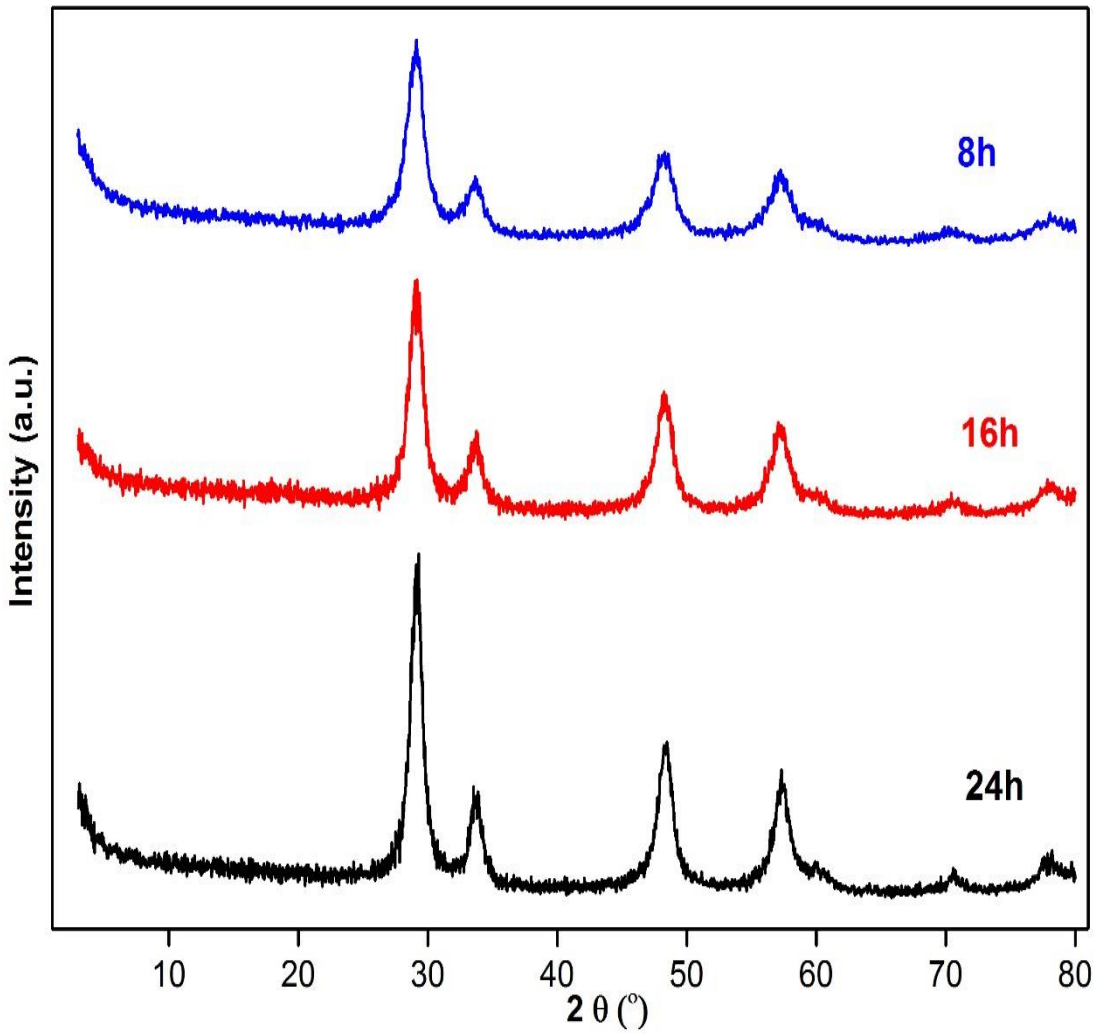

Figure 4.3. XRD patterns showing synthesis time effect on FeCoCZ_B for 8, 16 and 24 h.

4.2 Raman Spectroscopy.

Further analysis to determine the presence of amorphous oxides of Fe and Co was performed using Raman Spectroscopy technique. Information on molecular orbital (M-O) bond layout crystal structure, oxygen vacancies and lattice defects can be obtained via

Raman spectra. Ceria-zirconia nanocomposite with a space group of *Fm3m* and cubic fluorite structure is expected to have F_{2g} Raman band or active mode [73]. These structures comprise lattice vibrations of oxygen breathing mode which is significant to crystalline structure of the nanocomposites. The CZ Raman spectrum in Figure 4.4 showed a strong F_{2g} active mode at 461.06 cm^{-1} representing the breathing mode of oxygen ions connected to the cerium (Ce^{4+}) ions in the crystal lattice structure of CZ [72], [74], [75]. Co and Fe doped CZ nanocomposites exhibited different Raman spectra, lower band intensities and the inclusion of other peaks, when compared to CZ. This can be attributed to the presence of dopant ions in the lattice structure of CZ, exhibiting a Fe-Ce and Co-Ce linkage, leading to changes in their Raman spectra when compared to that of CZ [76]. Furthermore, the F_{2g} Raman band shift in positions is significant to change in lattice parameters and crystallite sizes causing oxygen signal vacancies and lattice distortions. Raman spectra exhibited by CoCZ and FeCoCZ_B showed a shift in the major F_{2g} active mode to a lower frequency band (459 cm^{-1}) as shown in Figure 4.5. This shift is significant to the longer Ce-O bond length which was as a result of the reduced lattice distortions in the lattice structure. Consequently, oxygen vacancies are generated to make-up for the substitution of Ce^{4+} with Fe and Co ions, thereby balancing the ionic charges [72]. This invariably leads to an increase in the OSC as a result of the generated oxygen vacancies.

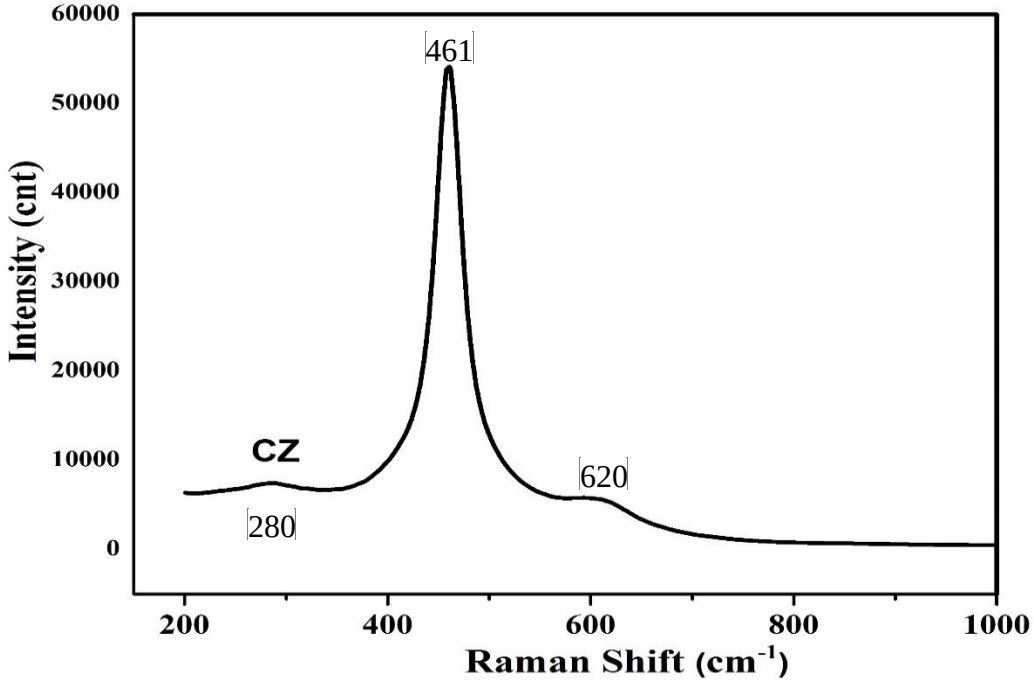

Figure 4.4. Raman Spectrum for ceria-zirconia.

FeCZ and FeCoCZ_A showed similar Raman spectra with a very reduced active mode F_{2g} band around 459 cm^{-1} (see Figure 4.5). This is probably as a result of high

composition of Fe in both nanocomposites and high content of amorphous Fe oxide on the surface of the crystalline structure of the nanocomposites. Consequently, Laguna et al explained that the reduced Raman peaks indicates a distortion in the lattice structure of the CZ due to the presence of dopants ions (Fe^{3+} and Co^{2+}) [75], which is significantly evident at compositions greater than 5 % doping. CoCZ, FeCZ, FeCoCZ_A and FeCoCZ_B exhibited minor peaks around 287 and 593 cm^{-1} which is similar to the minor peaks observed in the Raman spectra of CZ at Raman bands of 280 and 620 cm^{-1}. The presence of minor peaks in the doped samples of CZ can be attributed to the presence and interaction of Ce-Zr, Fe-Zr and Co-Zr linkages in their lattice structures, leading to the formation of tetragonal phase solid solutions [74], [75]. Furthermore, in the work carried out by Kang et al, tetragonal displacement of oxygen ions from the structural position in the cubic structure and the increased rearrangement of the anion sublattice was attributed to the presence of these weak bands in Raman spectra [77]. As a result, it can be inferred that lattice distortion in similarity to tetragonal phase formation is influenced by doping.

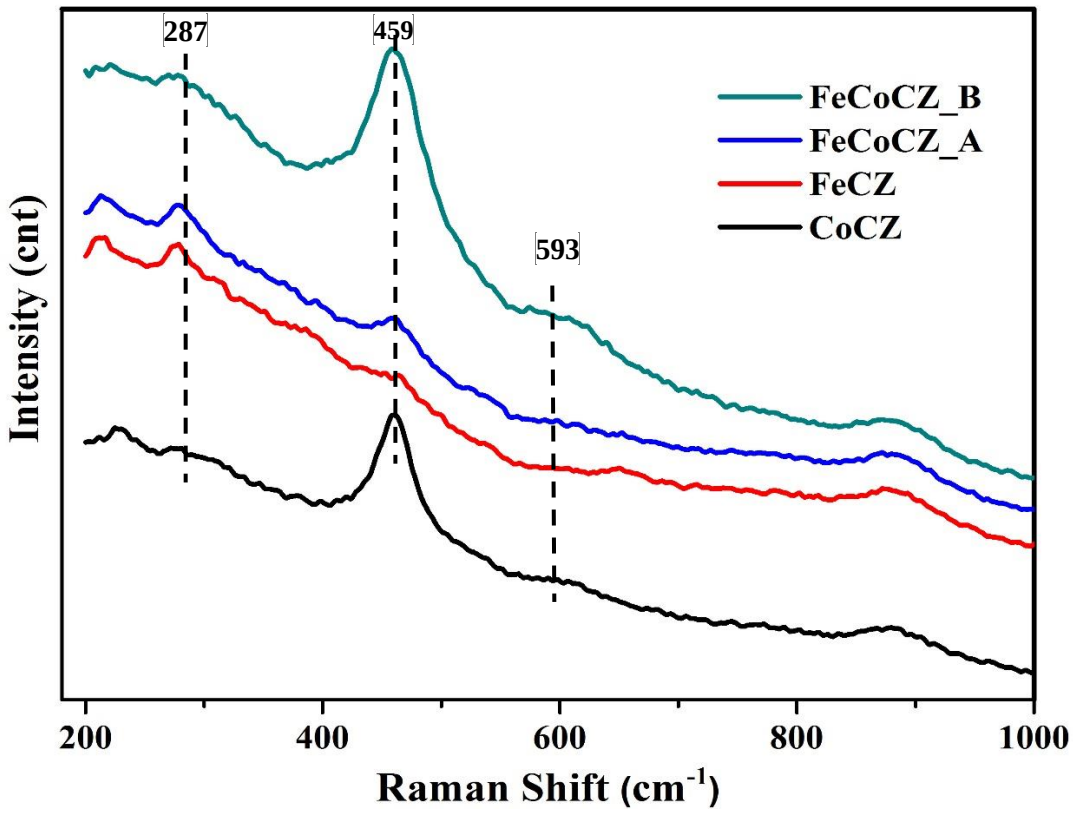

Figure 4.5. Raman spectra showing bands for FeCZ, CoCZ, FeCoCZ_A and FeCoCZ_B.

4.3 Analysis of Surface Morphology.

Crystalline morphology of the surface structure of the prepared nanocomposites were carried out using FE-SEM analytic technique. The prepared Fe and Co doped nanocomposites showed dense nanoparticle agglomeration as shown in Figure 4.6. The prepared samples are expected to have moderate or low level of porosity, due to the presence of interstitial spaces within the nanoparticle agglomerations of the ceria-zirconia nanocomposites acting as pores. However, critical examination of the SEM images revealed sparse nanoparticle agglomeration in CoCZ while CZ, FeCZ, FeCoCZ_A and FeCoCZ_B exhibited dense agglomeration. In other words, the nanoparticle agglomerations observed in the samples can be attributed to the effect of dehydration upon calcination, thereby causing weak or strong interactions depending on the nanoparticle agglomerations. Furthermore, spherical-shaped nanoparticles were observed in the morphology of CZ while the doped samples exhibited roughly-shaped spherical nanoparticles.

Thus, the nanoparticle shape observed in Fe and Co doped CZ highlights the presence and effect of dopant ions in the crystalline structure of the parent sample, as well as their effect on the surface structure and other morphological properties. Also, the smaller ionic radii of Fe and Co ions may influence the particle size diameter, thereby affecting the shape as a result of varied ionic radii within the crystal structure of the nanoparticles of the doped nanocomposites.

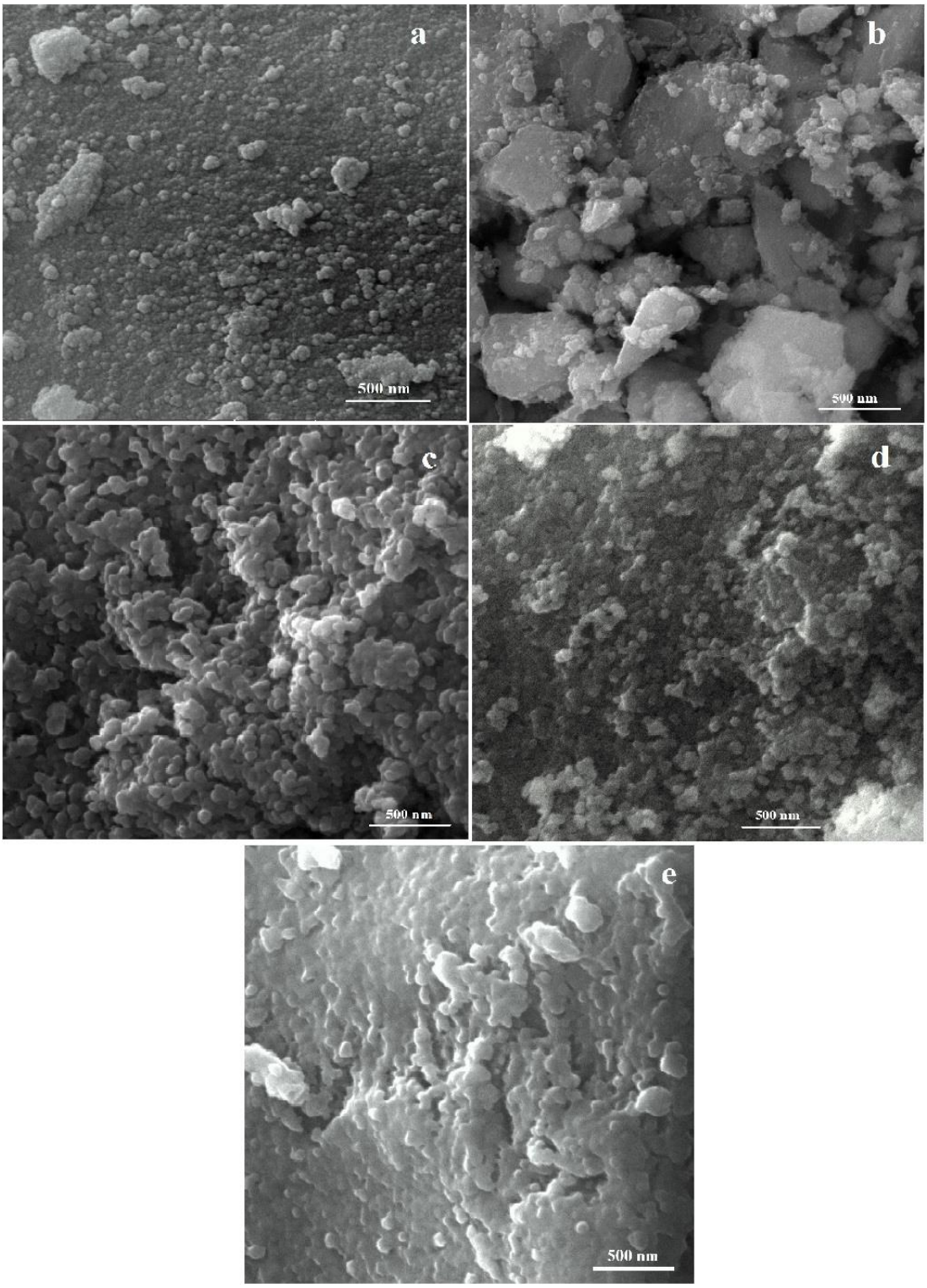

Figure 4.6. SEM Images of (a) CZ (b) CoCZ (c) FeCZ (d) FeCoCZ_A and (e) FeCoCZ_B nanocomposites.

4.4 Analysis of Physicochemical Properties.

Brunauer-Emmett-Teller (BET) surface area analyzer using N_2-adsorption technique was employed in analyzing the surface area of the prepared CZ nanocomposites. From the results obtained, the prepared samples were mesoporous and this is supported by the hysteresis loop formed by the adsorption-desorption isotherm plot, as shown in Figure 4.7. The analysis results displayed in Table 4.2 showed a reduced BET surface area (23 m^2/g) when CZ is doped with Co, while the BET surface area increases when doped with Fe. Furthermore, the results showed that the higher the Fe composition in the doped samples, the higher the BET surface area, average pore size, total pore volume and micropore volume. However, an indirect proportionality was observed in the case of Co doping. BET surface area, average pore size, total pore volume and micropore volume were reduced for the Co-doped CZ nanocomposite. Also, from Table 4.2, it can be observed that the average pore size, total pore volume and micropore volume of the prepared nanocomposites are in the order FeCoCZ_A > FeCZ > FeCoCZ_B > CZ > CoCZ. FeCoCZ_A has the largest BJH desorption average pore size, micropore volume and total pore volume. The distribution of the BJH desorption average pore sizes of the prepared samples are shown in Figure 4.8. These samples showed uniform size distribution except CoCZ which has two peaks at pore width points of 0.32 and 0.43 nm Å respectively. The largest pore width was observed in FeCoCZ_A between the points 5.2 – 14.6 nm. CZ and CoCZ showed lower average pore size, surface area and pore size distribution compared to FeCZ, FeCoCZ_A and FeCoCZ_B. A possible explanation for this contrast is the presence of Fe which enhances larger pore diameters in the Fe-doped samples, invariably leading to larger pore size and increased surface area.

Table 4.2. BET Surface Area, Pore Volume and Pore Size Analysis of CZ and Doped-CZ Nanocomposites.

Sample	S_{BET} (m^2/g)	V_{TOTAL} (cm^3/g)	V_{MICRO} (cm^3/g)	V_{MESO} (cm^3/g)	Average Pore Size (nm)
CZ	32	0.053	0.0004	0.052	4.217
CoCZ	23	0.045	0.0008	0.044	4.317
FeCZ	47	0.139	0.0019	0.137	8.825
FeCoCZ_A	43	0.173	0.0021	0.171	11.790
FeCoCZ_B	43	0.091	0.0016	0.089	5.960

[a] *S_{BET}: BET Surface Area;*
[b] *V_{TOTAL}: Total Pore Volume;*
[c] *V_{MICRO}: Micropore Volume;*
[d] *V_{MESO}: Mesopore Volume.*

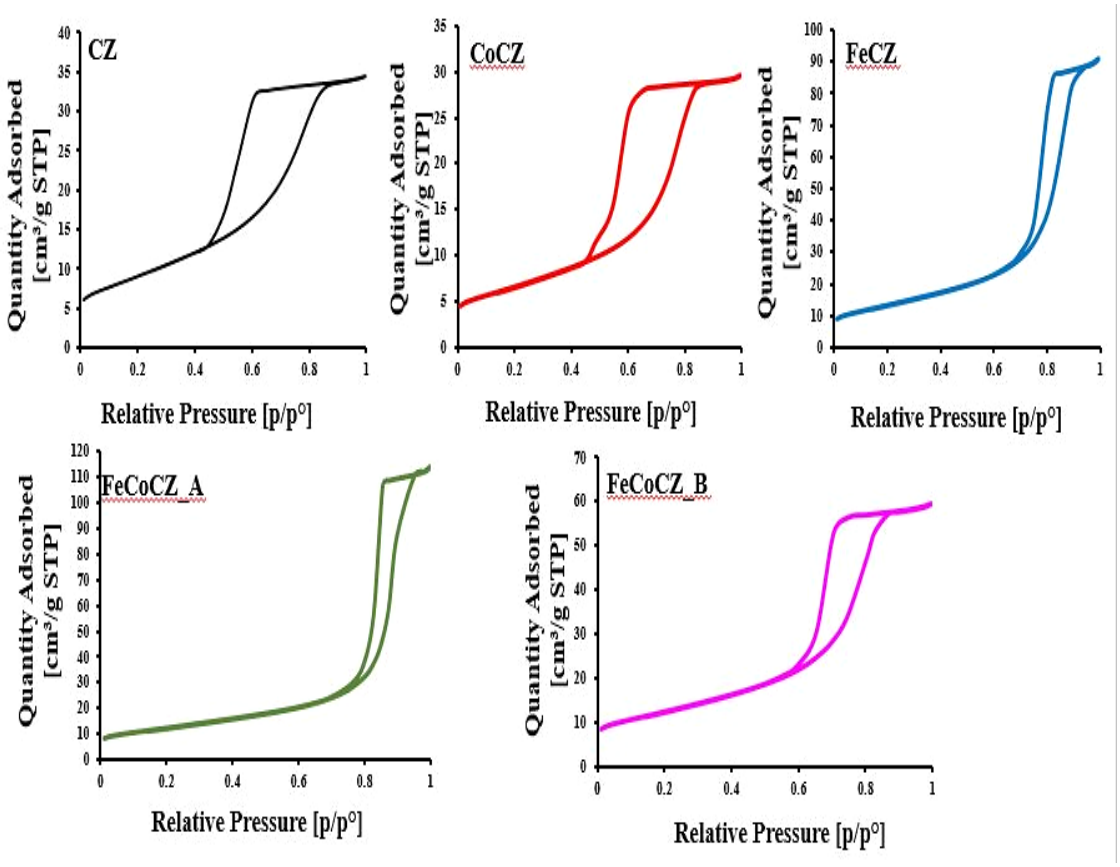

Figure 4.7. Adsorption-desorption isotherm plot for prepared (a) CZ (b) CoCZ (c) FeCZ (d) FeCoCZ_A and (e) FeCoCZ_B Nanocomposites.

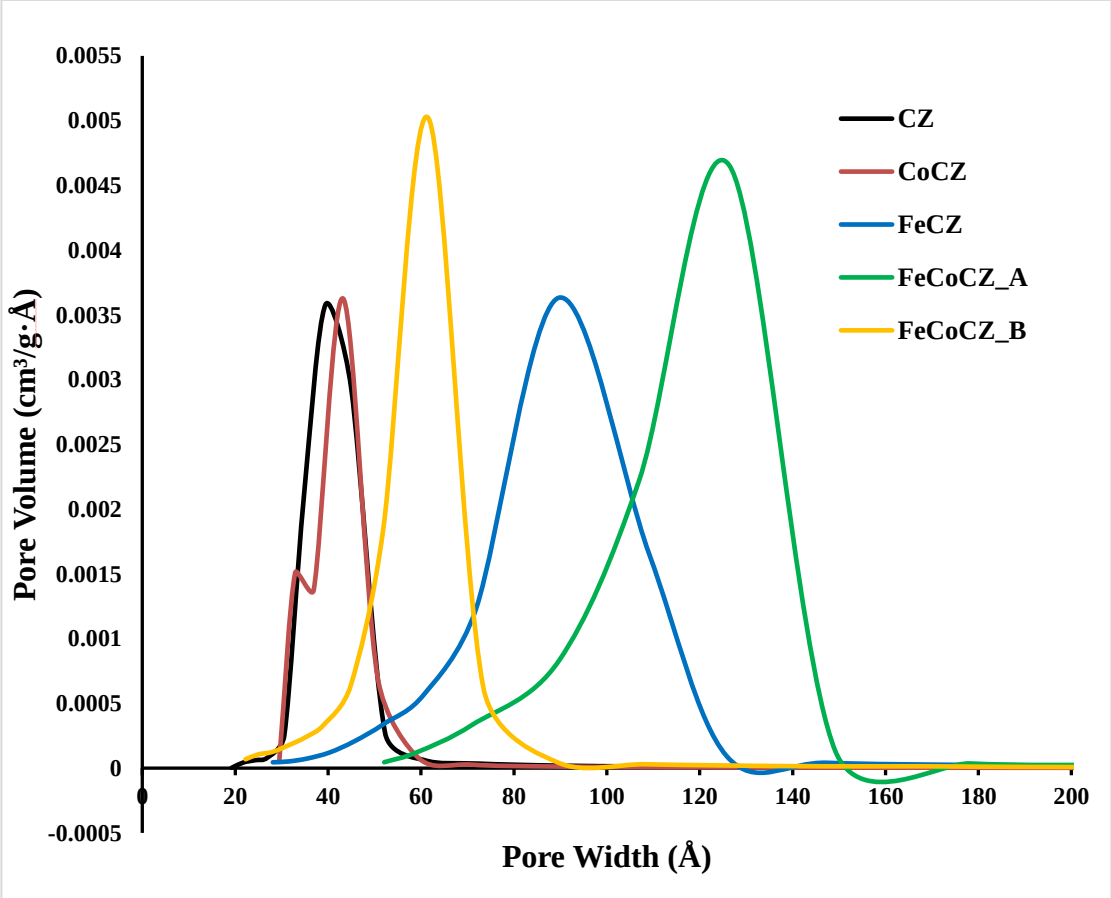

Figure 4.8. Graph showing Pore Size Distribution of the prepared CZ Nanocomposites.

Also, the large pore size observed in FeCZ and FeCoCZ_A can be attributed to the crystal lattice distortions observed in both sample, which is evident in their similar Raman spectra. However, doping with Co leads to shrinking of the pores within the CZ nanocomposites.

Effect of synthesis time variation on the morphology of FeCoCZ_B was also carried out. The results shown in Table 4.3 indicate that surface area, total pore volume and mesopore volume increases with increase in synthesis time. Highest micropore volume was obtained at 24 h synthesis time, while the same micropore volume was obtained at 8 and 16 h synthesis time variation. The average pore size distribution was also investigated as shown in Figure 4.9. Uniform pore size distribution was observed for all cases while the largest average pore size distribution was obtained at 16 h synthesis time.

Table 4.3. Effect of Synthesis Time Variation on Surface Morphology of FeCoCZ_B

Synthesis Time (h)	S_{BET} (m^2/g)	V_{TOTAL} (cm^3/g)	V_{MICRO} (cm^3/g)	V_{MESO} (cm^3/g)	Average Pore Size (nm)
8	25	0.062	0.0015	0.060	5.87
16	30	0.075	0.0015	0.073	7.06
24	43	0.091	0.0016	0.089	5.96

[a] *S_{BET}: BET Surface Area;*
[b] *V_{TOTAL}: Total Pore Volume;*
[c] *V_{MICRO}: Micropore Volume;*
[d] *V_{MESO}: Mesopore Volume.*

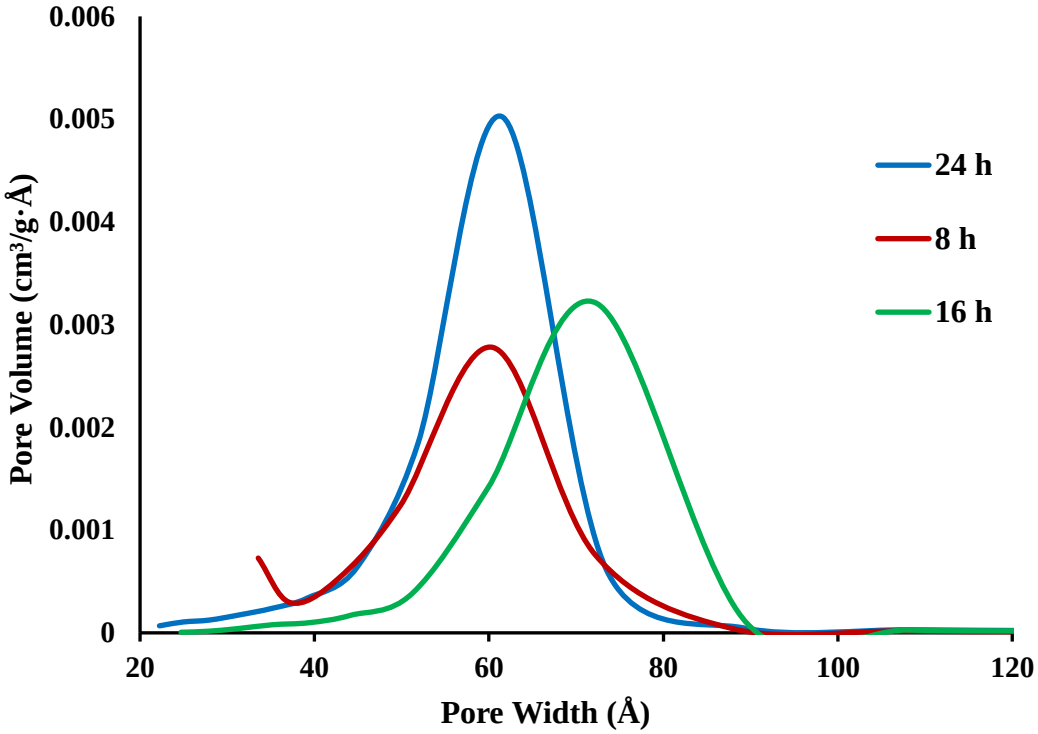

Figure 4.9. Pore Size Distribution for Synthesis Time Variation on Synthesis of FeCoCZ_B.

4.5 Acidity and Basicity Measurement.

The presence of acid and basic sites on the prepared samples were investigated using N_2-adsorption TPD technique. NH_3- and CO_2-TPD was carried out to investigate the presence of acid and basic sites respectively, on all the prepared CZ nanocomposite. The strength and distribution of acid and basic sites are significant to the catalytic performance of these nanocomposites. The knowledge of the strength, type and distribution of these sites helps in the optimization of these nanocomposites for selective and desired reactions. TPD experiment can remarkably differentiate the sorption energy level or strength of acid or basic sites into weak, medium or strong, however, details about the type of site cannot be determined such as the presence of Bronsted or Lewis acid site [78]. From CO_2-TPD in Figure 4.10, the strength of the basic sites is categorized into weak (40 – 300 °C), medium (310 – 500 °C) and strong (> 500 °C) basic sites. All the samples exhibited weak basic sites. CZ and CoCZ exhibited similar basic site distributions, each of them having weak basic sites depicted by desorption peaks at 84 °C ad 93 °C respectively. Furthermore, the presence of two peaks between 100 – 400 °C in the CO_2-TPD profile of FeCZ is associated with weak basic sites. FeCoCZ_B exhibited the presence of mostly weak basic sites, between 40 - 400°C. In addition, FeCoCZ_A showed the existence of basic sites in the whole experimental region from 40 – 900 °C, with significant presence of weak, medium and strong basic sites represented by strong desorption peaks.

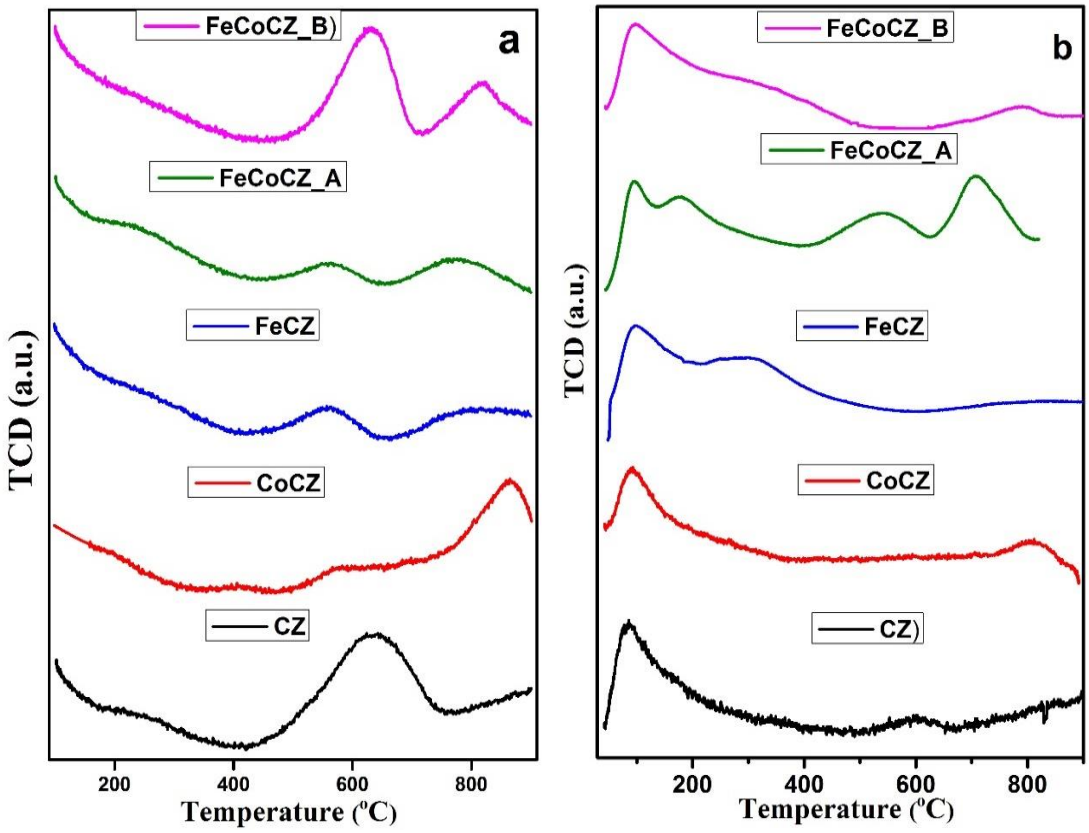

Figure 4.10. (a) NH_3-TPD and (b) CO_2-TPD of ceria-zirconia nanocomposites

From the NH_3-TPD profiles of the ceria-zirconia nanocomposites, all the Fe-doped samples have weak acid sites. Comparative study of the NH_3-TPD profiles of all the CZ nanocomposite samples, the rich acidity region of CZ and CoCZ showed the presence of a single peak. Also, from Table 4.4, the total acidity of all the prepared samples was low, with FeCoCZ_B having the largest total acidity value. In addition, we noticed that the total acidity of CoCZ was higher than the total basicity but, all other nanocomposite samples exhibited significantly lower total acidity than their basicity. Hence, from the results obtained, doping Co and Fe ions into the CZ lattice structure improves its acidity. This is evident in the calculated total acidity of the doped samples.

Table 4.4. Total Acidity and Basicity Estimation of Prepared Nanocomposites

Sample	Total Basicity (mmol g^{-1})	Total Acidity (mmol g^{-1})
CZ	0.43	0.066
CoCZ	0.28	0.68
FeCZ	20.77	0.57
FeCoCZ_A	13.76	0.51
FeCoCZ_B	3.20	0.76

4.6 Fourier Transform Infrared Radiation (FT-IR).

FT-IR spectra obtained for the prepared CZ nanocomposites are shown in Figure 4.11. The doped samples showed similar IR spectra but different from that of CZ which has two major peaks. However, FeCZ, FeCoCZ_A and FeCoCZ_B have more peaks with higher intensity in their spectra, when compared to CoCZ spectrum. The absorption band at 756 cm^{-1} in CZ spectrum as well as 550 – 650 cm^{-1} band range in the spectra of doped nanocomposites are significant to the skeletal bond vibration of metal-oxide [26–28]. In addition, adsorption bands at 980 cm^{-1} and 1100 cm^{-1} were present in the CZ and doped nanocomposite spectra respectively. These bands can be attributed to the vibrations of C-O stretching [79] and the influence of dopant ions on CZ lattice structure exhibits a shift to higher wavenumbers of the absorption bands. Also, the CZ-doped nanocomposites showed the presence of Ce-OH stretching and hydroxyl group bending vibrations at 1330 and 1640 cm^{-1} respectively, due to absorption of water molecules [27, 28]. We also observed that the iron-doped CZ nanocomposites exhibited metal oxide vibrations at 1500 cm^{-1} which can be attributed to OH-group bending vibrations. Both CoCZ and FeCoCZ_B showed broadband with absorption peak at 3420 cm^{-1}. This can be attributed to the hydroxyl group stretching vibration [40], due to the physical absorption of water .

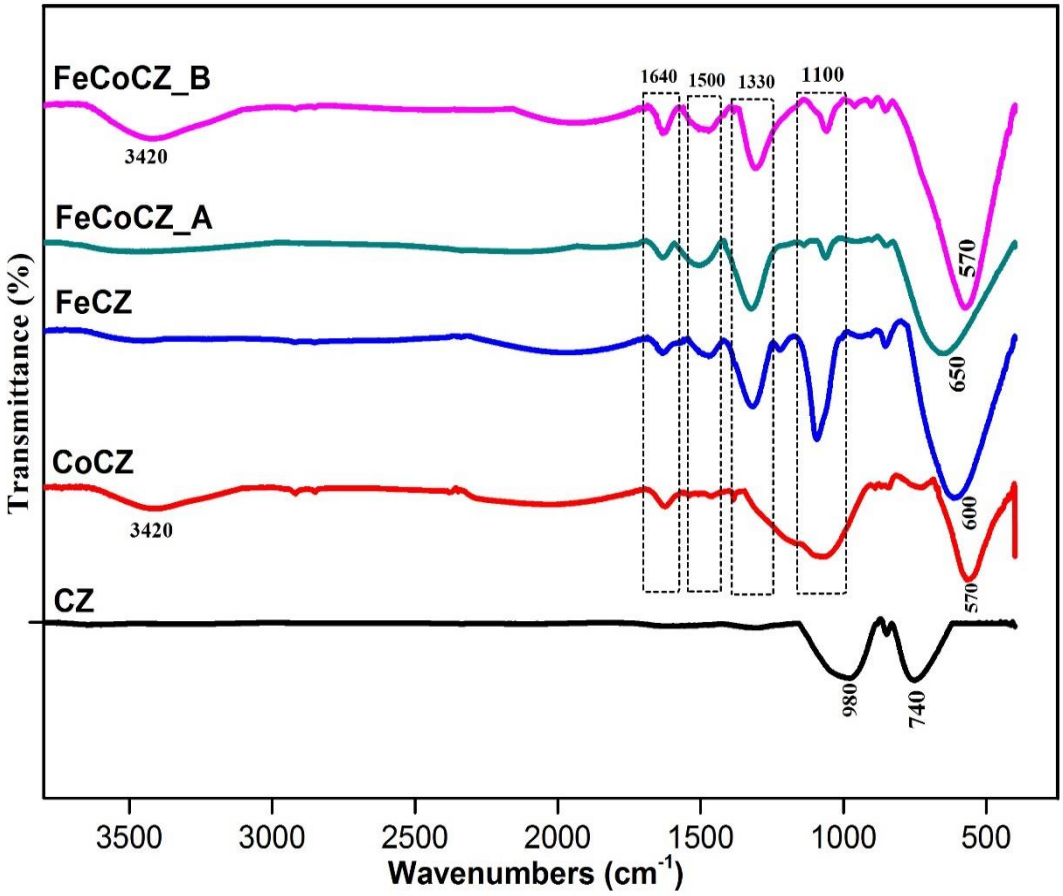

Figure 4.11. FTIR spectroscopy of CZ and doped nanocomposite samples

4.7 Pyridine-Adsorbed FT-IR spectroscopy.

Pyridine-adsorbed FT-IR was carried out on the CZ nanocomposites to obtained more characteristic information on their surface acidity. All the nanocomposites exhibited broad bands associated with Lewis acid sites due to the bonding or molecular absorption of pyridine on Ce^{4+}, Zr^{4+}, Fe^{3+} and Co^{2+} cations (see Figure 12). The spectra were obtained initially at 423 K and further outgassed to 523 K to observe the effect of temperature on the absorption bands intensity and their shift in position to lower or higher wavenumbers. CZ exhibited bands at 1606, 1500 and 1455 cm^{-1} positions. The strong band centered at peak position 1606 cm^{-1} is significant to 8a $\nu_{c\text{-}c}$ [81], [82] vibrational mode and can be assigned to zirconia (ZrO_2), as a result of adsorbed pyridine on Zr^{4+} with the absence of a shoulder peak at 1597 cm^{-1} [39]. The other absorption bands of 1500 and 1455 cm^{-1} can be attributed to 19a and 19b modes of bonded pyridine [81], [82]. The intensity of 1455 cm^{-1} band increased with outgassing temperature (523 K) and is significant carbonaceous species, due to cracking of adsorbed pyridine on Lewis acid sites [39], [83]. However, the weak band at 1500 cm^{-1} fades at 523 K. CoCZ exhibit two peaks significant to 19a and 19b with a shift in position of the two peaks after outgassing to 523 K. In addition, FeCZ exhibited single peak positioned at 1619 cm^{-1} which shifts to 1625 cm^{-1} after outgassing to 523 K. FeCoCZ_A and FeCoCZ_B exhibited similar spectra to that of CZ with stronger intensity bands. The broad band at 1599 cm^{-1} of FeCoCZA spectrum collected at 423 K (8a vibrational mode) shifts to 1605 cm^{-1} after outgassing to 523 K. The absorption band centered at 1473 cm^{-1} increased and shifted to a slightly higher wavenumber of 1475 cm^{-1} after outgassing to 523 K. In addition, the 19b vibrational mode at 1441 cm^{-1} shifted to a lower wavenumber (1434 cm^{-1}) with increased band intensity. Observations made from FeCoCZB spectrum, absorption band at 1606 shifted to 1608, after outgassing from 423 K

to 523 K, with reduced peak intensity. However, after outgassing to 523 K, the peaks at 1473 and 1441 cm^{-1} shifted to lower absorption bands of 1471 and 1434 cm^{-1} with increased vibrational mode intensities, respectively. Overall, all the catalysts samples exhibited Lewis acid bonded sites with vibrational mode, indicating that the prepared metal oxide solid solutions possess Lewis acidity.

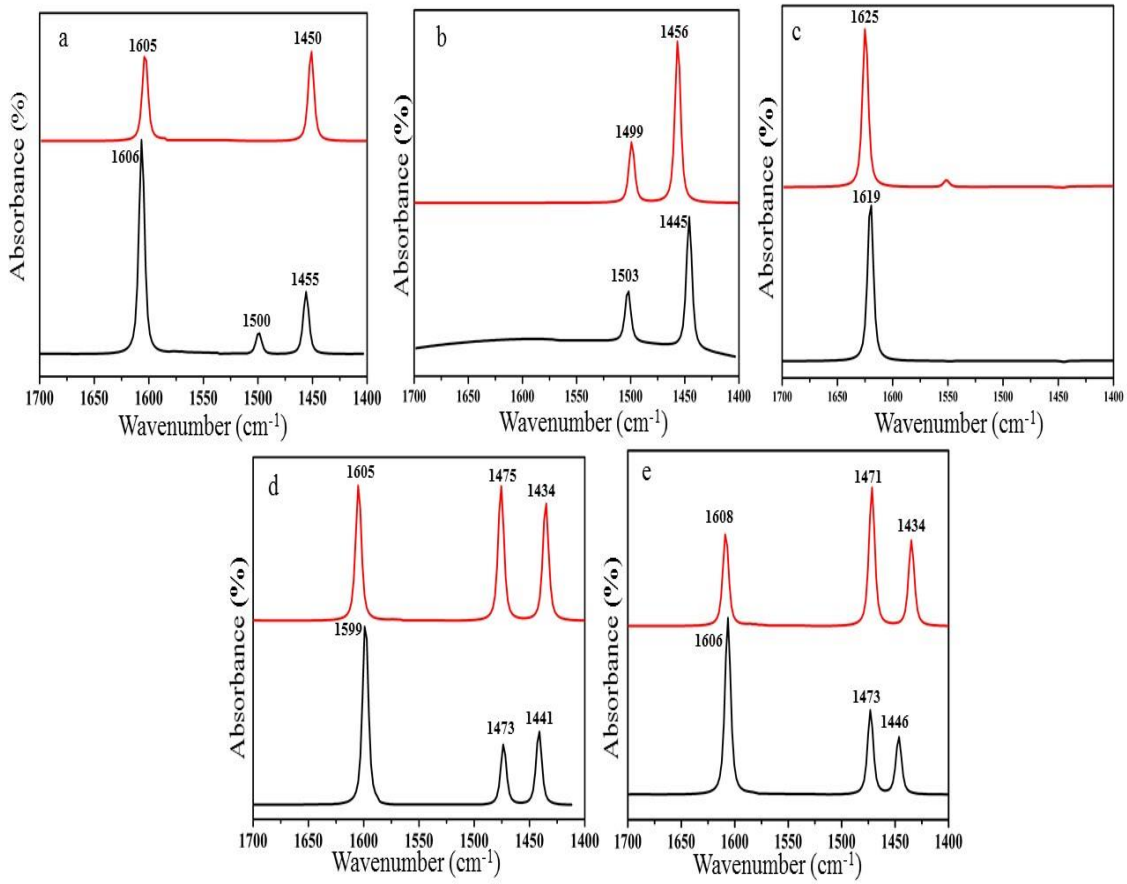

Figure 4.12. Pyridine-Adsorbed FT-IR spectra of (a) CZ (b) CoCZ (c) FeCZ (d) FeCoCZ_A and (e) FeCoCZ_B showing the presence of Lewis Acid Sites.

4.8 Thermogravimetric Analysis

Thermal stability of the prepared CZ nanocomposites was investigated using thermogravimetric analysis technique (TGA) in terms of weight loss versus temperature (see Figure 4.13). All the samples showed excellent stability with minimal weight loss in the selected temperature region, as shown in Table 4.5. Figure 4.13 shows that CoCZ, FeCoCZ_A and FeCOCZ_B all exhibited two weight loss steps which may be due to the presence of cobalt ions in their crystal lattice structure, while CZ and FeCZ both exhibited only one weight loss step. The first step can be attributed to the presence of water however, a shoulder step was found at 46 °C for FeCZ TG curve. The small weight loss of the samples shows that the ceria-zirconia nanocomposites solid solutions were formed by hydrothermal treatment in the synthesis process [84], and not by calcination. This is evidently supported by the XRD profiles of all the samples (see Figure 4.1 and 4.2) before calcination treatment, showing the formation of cubic phase structure with no extra peaks.

Table 4.5. Weight loss of CZ nanocomposites at 200 °C, 600 °C and 950 °C from TGA curves

Samples	Weight (%)		
	200 °C	**600 °C**	**950 °C**
CZ	2.31	2.77	2.95
CoCZ	1.74	2.02	2.94
FeCZ	1.72	2.4	2.55
FeCoCZ_A	2.34	2.77	3.73
FeCoCZ_B	2.27	2.76	3.30

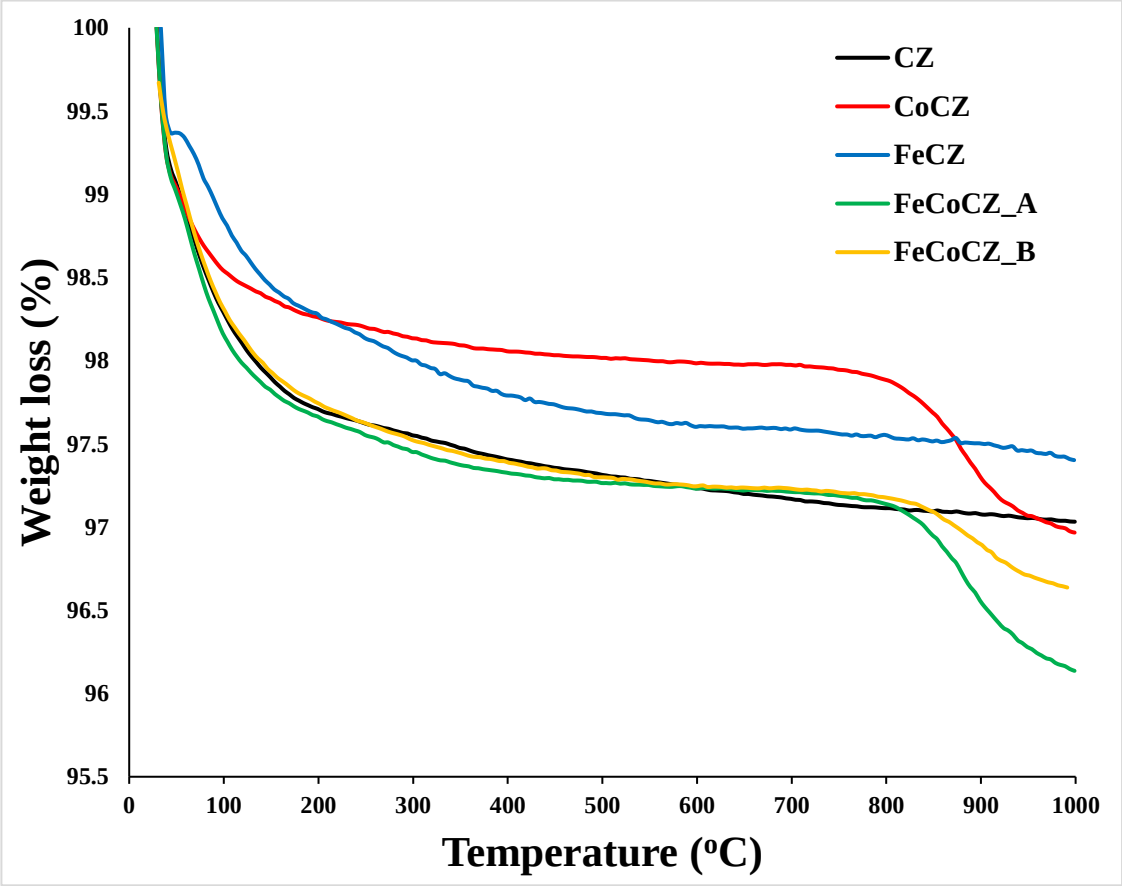

Figure 4.13. TG curves showing thermal stability of CZ nanocomposites in terms of weight loss.

4.9 Catalytic Cracking of Hexane

Schematic diagram of the fixed bed reactor setup is shown in Figure 4.14, highlighting the reactor components and working conditions during the catalytic cracking of n-hexane via the prepared CZ nanocomposites.

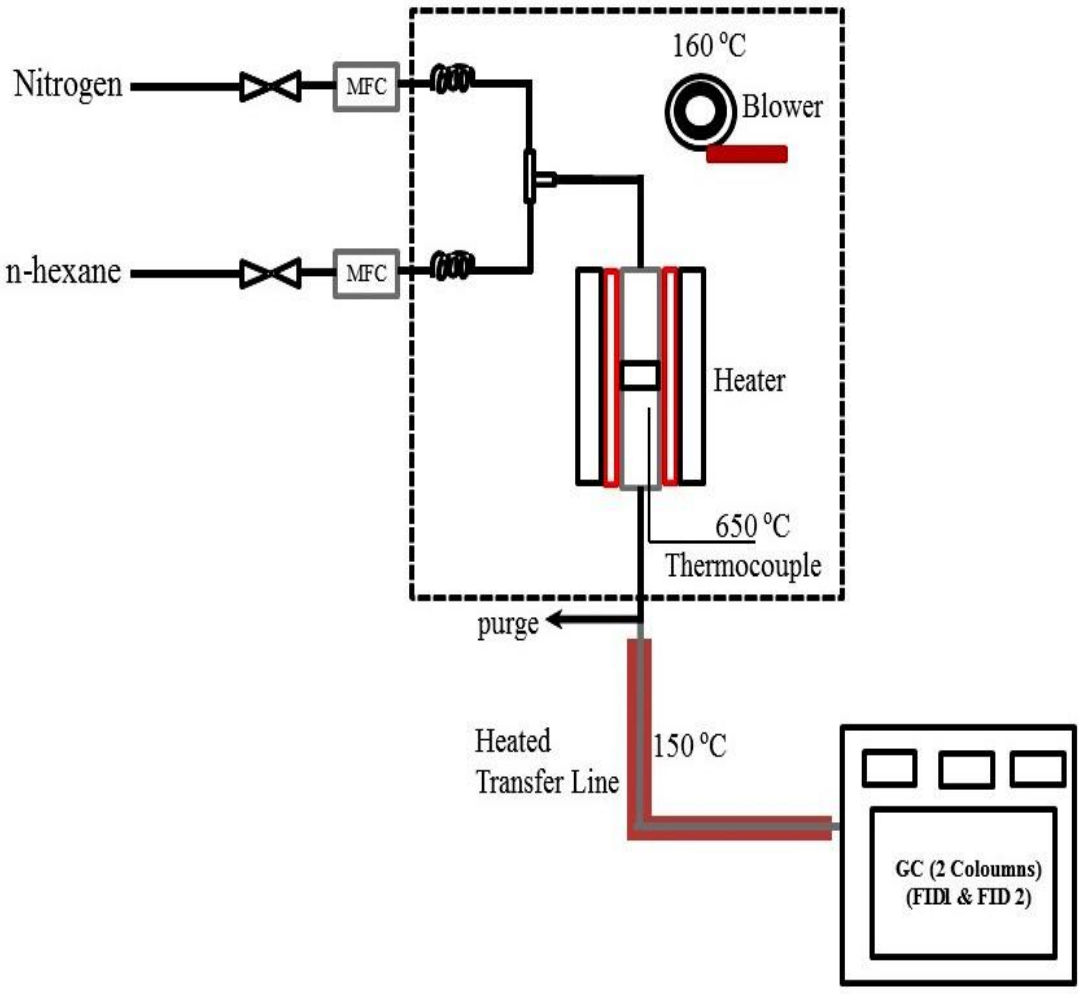

Figure 4.14. Schematic Diagram of Fixed-Bed Reactor Setup

4.9.1 Activity of CZ nanocomposites in catalytic cracking of n-Hexane

The synthesized ceria-zirconia nanocomposite catalyst was tested for hexane cracking at a feed flow composition of of 17.5% hexane feed + 82.5% N_2, at temperature of 650 °C, and W/F of 0.087 h. The doped samples were also tested at these same conditions to investigate the influence of dopant ions on the performance of ceria-zirconia in catalytic cracking of n-hexane. The results obtained are reported in Table 4.6 and Figure 4.15, outlining the initial conversion, selectivity and selected products yield, and subsequent results after 5 h and 10 h reaction time for each catalyst.

The doped nanocomposite catalysts exhibited higher initial (at 1 h) conversion than CZ. Highest selectivity to ethylene and propylene olefins was exhibited by CZ over 10 h time-on-stream. Both CoCZ and FeCZ gave highest initial conversions approximately 83% and CoCZ gave the highest initial total selectivity of 89.6 % to olefins. However, very low initial selectivity to C_2 and C_3 olefins was observed, which was remarkably improved and stable between 5 and 10 h time-on-stream as reported in Table 4.6. FeCZ gave the lowest initial selectivity to olefin and high paraffin selectivity in comparison with other catalyst samples. Improvement was observed over reaction time-on-stream, with both CoCZ and FeCZ catalysts showing increased total olefin selectivity which may be explained by the further β-splitting or dehydrogenation of the intermediates or products formed by isomerization.

Table 4.6. Performance of CZ and CZ nanocomposite catalysts on n-hexane cracking (Testing conditions: 650 °C, 17.5 % n-hexane, 82.5 % N_2 W/F = 0.087 h and 0.3 g catalyst loading)

Catalyst	TOS (h)	Conv (mol %)	Light Olefins Selectivity (%)			Paraffin Selectivity			BTX (%)
			$C_2^=$	$C_3^=$	Others	C_1	C_2	Others	
CZ	1	31.2	35.2	33.8	5.8	13.1	9.7	2.2	0.2
	5	23.9	35.4	33.9	5.3	13.3	9.8	2.3	0.0
	10	21.5	36.0	33.9	4.8	13.3	9.8	1.9	0.3
CoCZ	1	82.7	8.5	8.6	72.5	3.2	2.4	3.1	1.7
	5	29.7	27.4	29.7	14.9	12.1	11.1	3.7	1.1
	10	28.5	28.5	30.3	9.8	13.4	11.7	3.9	2.4
FeCZ	1	83.1	20.5	26.1	8.2	12.1	12.7	12.2	8.2
	5	22.8	35.2	34.2	4.5	13.4	10.3	2.2	0.2
	10	21.0	35.5	33.8	5	13.3	10.1	2.0	0.3
FeCoCZ_A	1	49.0	34.0	31.8	7.0	14	10.9	2.0	0.3
	5	41.7	34.5	31.9	7.1	13.5	10.1	2.0	0.9
	10	33.3	34.8	32.7	6.1	13.5	10.3	2.3	0.4
FeCoCZ_B	1	32.4	31.9	28.9	12.8	12.9	9.4	2.4	1.7
	5	24.5	34.5	33.0	6.1	13.4	10.7	1.8	0.5
	10	20.2	34.5	33.8	5.2	13.3	10.7	2.3	0.2

TOS: Time-on-stream
Conv: n-hexane conversion
BTX: Benzene+Toluene+Xylene selectivity
C_1: methane
C_2: ethane
$C_2^=$: ethylene
$C_3^=$: propyylene

Both CoCZ and FeCZ exhibited reduced stability during reaction over 10 h TOS. This was evident in the rapid drop of hexane conversions over 10 h reaction time-on-stream. This was due to rapid coking and the possible deactivation of active sites on CoCZ and FeCZ during the catalytic reaction. Also, large amount of coke deposition which may have covered large portions of available pores and active sites, is also responsible. Furthermore, the higher loading compositions (20 wt.%) of Co and Fe on CZ may be responsible for the high initial conversion but subsequent low conversions and stability of both catalysts, with time.

CZ, FeCoCZ_A and FeCoCZ_B exhibited conversions with improved stability over 10 h reaction time as reported in Table 4.6, although, with lower initial conversions compared to FeCZ and CoCZ. CZ and FeCoCZ_A also exhibited significantly stable selectivity towards ethylene and propylene as compared with other catalysts. Furthermore, CZ, FeCoCZ_A and FeCoCZ_B showed stable initial and subsequent C_1 and C_2 paraffin selectivity over 10 h time-on-stream. Figure 4.15 shows that FeCoCZ_A exhibited stable total olefins selectivity and highest ethylene and propylene yield after 10 h reaction time. Thus, better catalytic performance and stability was obtained with CZ doped with both Fe and Co, 10% each. However, analysing the obtained results, FeCoCZ_A (10 wt.% Fe and Co each) gave better catalytic activity and performance than FeCoCZ_B (5 wt.% Fe and Co each). This may be due to higher loading compositions of the dopant ions in FeCoCZ_A catalyst and its higher total basicity. Comparatively, FeCoCZ_A exhibited the best catalytic performance according to the results in Table 4.6. This is evident in its high stability and conversion over time-on-stream, high ethylene and propylene selectivity, as well as high combined yield of ethylene and propylene even after 10 h. This can also be supported by

characterization results, with FeCoCZ_A having the highest pore size and distribution, and enhanced Lewis acid sites by pyridine adsorption, invariably enhancing its high available active sites needed for reaction. Moreover, we can possibly infer that increasing the loading composition of Fe and Co on CZ nanocomposite catalyst improves its catalytic performance. However, increased loading above 10% may reduce catalytic performance of doped CZ nanocomposite.

Comparatively, promoting ceria-zirconia with dopant ions of Fe and Co improves` the cracking of the C-H bond leading to better n-hexane conversion, in the first 5 h TOS except for FeCZ with the lowest conversion at 5 h reaction time.

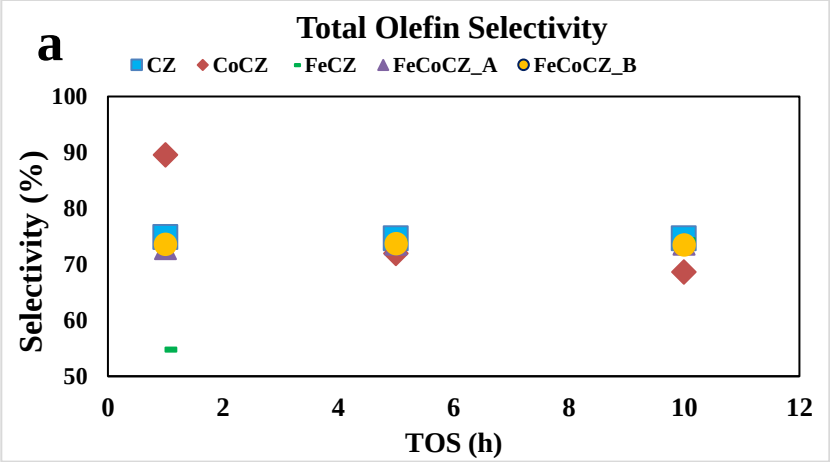

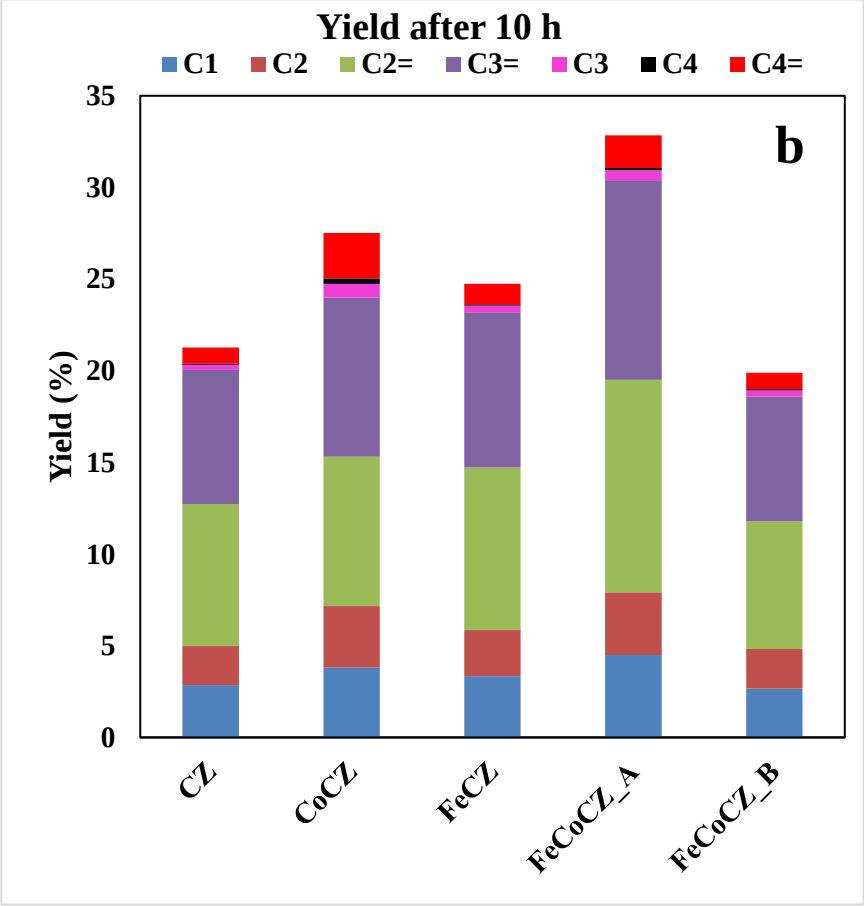

Figure 4.15. (a) Total olefin selectivity and (b) C_1, C_2, $C_2^=$ and $C_3^=$ yield after 10 h time-on-stream.
Reaction conditions: 650°C, W/F = 0.087 h, 0.3 g catalyst and 17.5% Hexane + 82.5% N_2 feed flow

4.9.2 Temperature Variation Effect on performance of FeCoCZ_A

Based on the performance comparison, FeCoCZ_A gave the best catalytic activity according to the results reported in Section 4.2. Thus, we studied the influence of temperature variation on cracking of n-hexane and product distribution over FeCoCZ_A. Catalytic activity was exhibited at both reported temperatures, with improved performance obtained at 650 °C under the same reaction parameters. At 600 °C, FeCoCZ_A gave lower catalytic conversions over 10 h reaction time. In addition, the total olefin selectivity was lower with high methane yield, high BTX formation (Figure 4.16), and higher paraffin selectivity according to Table 4.7. Careful observations of the reported results show steady reduction in the overall olefin selectivity as well as product selectivity of ethylene and propylene over 5 h time-on-stream. However, a huge drop of 86.5% was observed in the total olefin selectivity after 10 h reaction time, which is noticeable in the significant reduction in $C_2^=$ and $C_3^=$ olefins selectivity after 10 h time-on-stream. On the other hand, overall paraffin selectivity increased steadily over the first 5 h reaction time, and a 53.3% significant increment after 10 h with 48.6 % methane selectivity. Thus, some olefins are lost to paraffin over time-on-stream.

Conversion and product selectivity followed a similar trend which was observed in the combined product yield reported in Table 4.7. C_2-C_3 olefin yield reduces with reaction time-on-stream while C_1-C_2 paraffin yield increased. This may be explained by the increasing aromatization and isomerization reaction of the formed intermediates on the catalyst surface to form more BTX and RCH_2 (paraffin) with time. Also, we may suggest the possible hydrogenation of olefins to paraffin, due to extensive exposure to metal ions on the available active sites, during the reaction.

Table 4.7. Effect of temperature and catalyst weight per feed flowrate (W/F) variation on conversion, selectivity and yield of FeCoCZ_A on n-hexane cracking.

	TOS (h)	Conv (mol %)	Light Olefins Selectivity (%)			Parafins Selectivity (%)			BTX (%)
			$C_2^=$	$C_3^=$	Others	C_1	C_2	Others	
Temperature Variations (°C)									
600	1	33.9	14.7	29.8	14.1	7.4	10.4	14.7	8.9
	5	23.1	17.2	24.5	10.6	13.2	14.9	8.3	11.3
	10	20.2	1.4	3.1	2.5	48.6	11.7	17.7	15
650	1	49.0	34.0	31.8	7.0	14.0	10.9	2.0	0.3
	5	41.7	34.5	31.9	7.1	13.5	10.1	2.0	0.9
	10	33.3	34.8	32.7	6.1	13.5	10.3	2.3	0.4
Catalyst weight per feed flowrate, W/F (h)									
0.131	1	25.8	35.7	30.5	8.8	11.2	6.2	6.3	1.3
	5	19.3	34.4	30.1	9.8	13.9	6.5	3.5	1.8
	10	18.6	35.6	28.3	11.1	14.7	5.9	2.6	1.8
0.087	1	49.0	34.0	31.8	7.0	14.0	10.9	2.0	0.3
	5	41.7	34.5	31.9	7.1	13.5	10.1	2.0	0.9
	10	33.3	34.8	32.7	6.1	13.5	10.3	2.3	0.3
0.065	1	78.1	22.3	29.8	9.2	15.2	14.8	7.7	1.0
	5	75.2	0.0	0.1	0.6	96.3	2.5	0.4	0.1
	10	57.4	0.1	0.1	1.1	98.4	0.1	0.0	0.2

TOS: Time-on-stream
Conv: n-hexane conversion
BTX: Benzene+Toluene+Xylene selectivity
C_1: methane
C_2: ethane
$C_2^=$: ethylene
$C_3^=$: propyylene

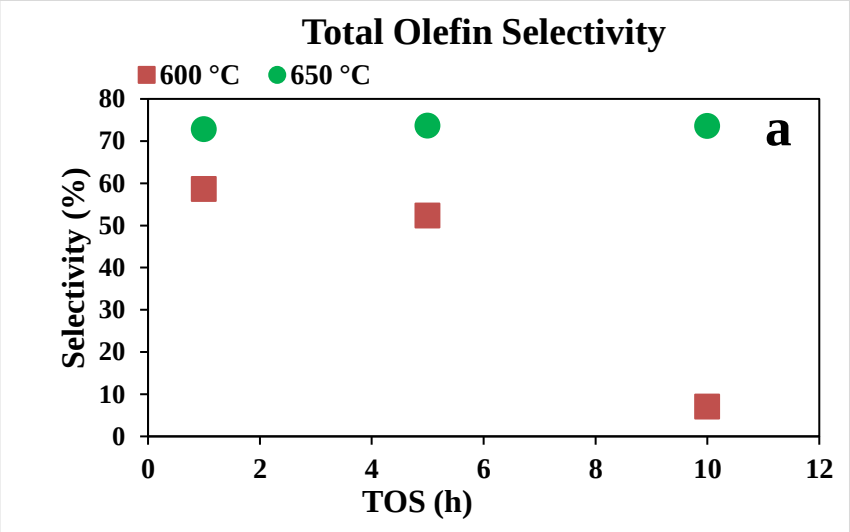

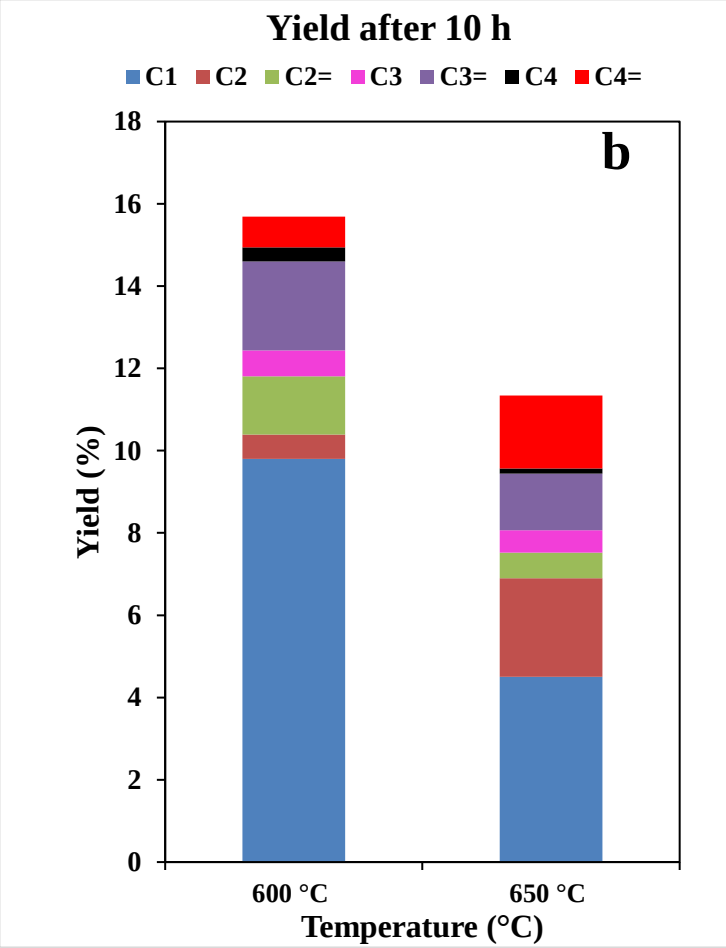

Figure 4.16. Effect of temperature variation on performance of FeCoCZ_A (a) Total olefin selectivity over TOS (b) C_1, C_2, $C_2^=$ and $C_3^=$ yield after 10 h time-on-stream.

Furthermore, ethylene selectivity was higher than that of propylene at 650 °C and vice versa at 600 °C, over the entire reaction time. According to Boyadjian *et al* [23], this is as a result of further cracking of C_3 and C_4 olefins to C_2 olefin at higher temperature. Also, C_2 olefin is mainly formed from monomolecular (or protolytic) cracking of carbenium-ions on acid sites which is supported by higher temperature [26]. Furthermore, Wang *et al* reported that C_2 olefin formation from carbenium-ions is not controlled by either monomolecular or bimolecular cracking mechanism at high temperature [24]. In addition, higher propylene formation and selectivity at 600 °C is probably significant to bimolecular chain cracking mechanism which is favoured by lower reaction temperature and hydride-transfer, followed by β-scission of the formed intermediate or carbenium-ion [20, 22].

4.9.3 Influence of catalyst weight per feed flowrate on performance of FeCoCZ_A

Effect of catalyst weight per feed flowrate (W/F) variation was studied by varying the n-hexane feed flow rate (0.02, 0.05 and 0.08 mL/min) at constant catalyst weight (0.3 g) and constant N_2 carrier gas flow. From the reported results in Table 4.7 conversion increases with decreasing W/F, over the entire time-on-stream. At W/F of 0.131 h and 0.087 h, we observed only slight difference in the olefin selectivity but similar trend and selectivity stability for ethylene and propylene. Considering product yield (see Figure 4.17), W/F of 0.087 h gave significantly higher $C_2^{=}$ - $C_3^{=}$ olefin as well as $C_1 – C_2$ paraffin combined yields (Figure 4.17). At W/F = 0.065 h which gave highest conversion, we observed lower ethylene and propylene selectivity initially, with high yield. However, at higher reaction time-on-stream, product selectivity towards ethylene and propylene was almost or approximately zero between 5 and 10 h time-on-stream.

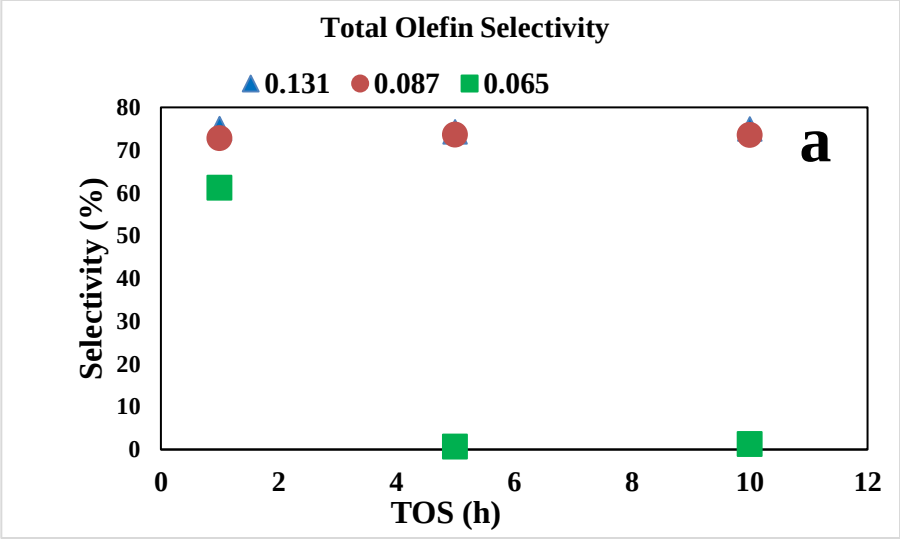

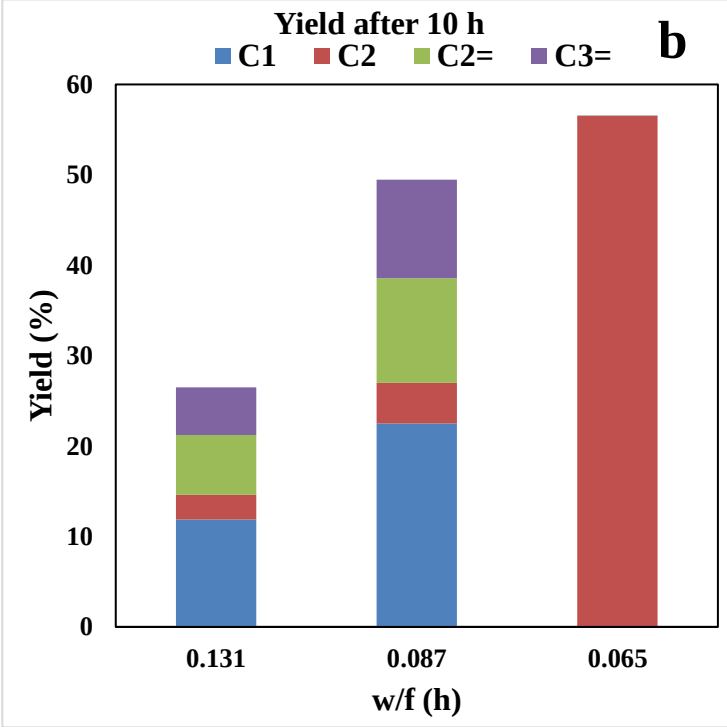

Figure 4.17. Effect of catalyst weight per feed flowrate (W/F) variation on performance of FeCoCZ_A (a) Total olefin selectivity over time-on-stream (b) C_1, C_2, $C_2^=$ and $C_3^=$ yield after 10 h time-on-stream.

This is because most of the olefins formed have been converted to paraffin as evident by the results shown in Figure 4.17b and Table 4.7 (56.45% methane yield). Also, total paraffin selectivity was approximately estimated to be 99% comprising 96.3 and 98.4% selectivity for methane after 5 h and 10 h reaction time-on-stream, respectively. Thus, to enhance favourable olefin selectivity, W/F should be greater than 0.065 h for this research study.

4.10 Regeneration and Reusability of Prepared Catalysts

For economic purposes and viability, a catalyst should possess regenerative properties for potential reusability and long life. The amount of coke deposited on FeCoCZ_A (48.1 %) was greater than that of CZ (8.5 %). This can be explained by the presence of Fe and Co ions incorporated into the lattice structure of FeCoCZ_A. Also, the presence of amorphous and filamentous carbon peaks was observed from XRD analysis performed on the spent samples of CZ and FeCoCZ_A, respectively. However, their phase structure remained unaltered (see Figure 4.18). Also, FE-SEM was performed to investigate the morphological changes of the spent catalysts. The obtained micrograph images showed presence of filamentous carbon rods and nanofibers on FeCoCZ_A while amorphous carbon was observed on spent CZ (see Figure 4.19).

The amorphous carbon observed on spent CZ was probably due to the adsorption of hexane on the metal ions on its active sites, leading to disintegration of the hexane feed to form carbon deposit with time [32, 33]. Also, the development of rods and fibrous-structured carbon deposited on spent FeCoCZ_A may be caused by the dissolution of n-hexane feed on the metal ions, enhancing the formation of filamentous carbon [32, 33]. Also, morphology and shape orientation of the nanoparticle is a major factor in the

formation of structured carbon deposit on FeCoCZ_A [85]. Furthermore, appreciable amount of filamentous carbon deposited on spent FeCoCZ_A were carbon rods and can be observed at 50 μm micrograph image scale (Figure 4.19). This is as a result of additional aggregation of amorphous carbon which were accumulated on the catalyst surface and reactor wall during the reaction time in a process known as thickening, according to Terry and Baker [85].

Both samples were regenerated by calcination at 600 °C for 4 h. XRD analysis of the regenerated samples exhibited no extra peaks, with similar patterns to that of the fresh samples. The results obtained are displayed in Figure 4.18 and 4.19, comparing the fresh, spent and regenerated CZ and FeCoCZ_A. In addition, the SEM micrographs after regeneration showed that no coke (carbon) deposition were present on the surface of both catalysts. In addition, detailed observation of the SEM images showed restored morphology of both samples after regeneration.

The regenerated FeCoCZ_A was reused for catalytic cracking of hexane (Table 4.8) and it exhibited catalytic activity with 9.1 % loss and 16.9 % loss in performance based on conversion, for first and second cycle run. The decreasing catalyst activity after regeneration can be attributed to the slow changes in the surface morphology of FeCoCZ_A. Metal oxides exhibit slight morphological changes and increased agglomeration due to thermal effect. This can be observed in the slight change of the nanoparticles shapes of the regenerated samples (see Figure 4.19) and the increasing nanoparticle agglomeration after each regeneration cycle via calcination. This increasing agglomeration will result to decrease in porosity hence, causing a gradual decline in the catalyst activity significant to loss of available active sites by pore constriction.

Table 4.8. Regenerative capability of FeCoCZ_A for two cycle regeneration runs on n-hexane cracking.

Cycle	TOS (h)	Conv (%)	Light Olefins Selectivity (%)			Parafins Selectivity (%)			BTX (%)	Yield (%)	
			$C_2^=$	$C_3^=$	Others	C_1	C_2	Others		$C_2^=+C_3^=$	$C_1+ C_2$
Fresh	1	49.0	34.0	31.8	7.0	14.0	10.9	2.0	0.3	32.2	12.2
	10	33.3	34.8	32.7	6.1	13.5	10.3	2.3	0.4	22.5	7.9
1	1	44.5	23.8	28.8	6.8	12.3	11.9	9.2	7.2	23.4	10.8
	10	33.5	33.8	32.9	6.8	13.4	10.4	2.7	0.0	22.4	8.0
2	1	41.7	30.5	30.8	8.2	13.8	12.0	0.2	4.5	15.2	7.8
	10	30.0	30.5	32.5	8.0	13.2	11.5	4.2	0.1	18.9	7.4

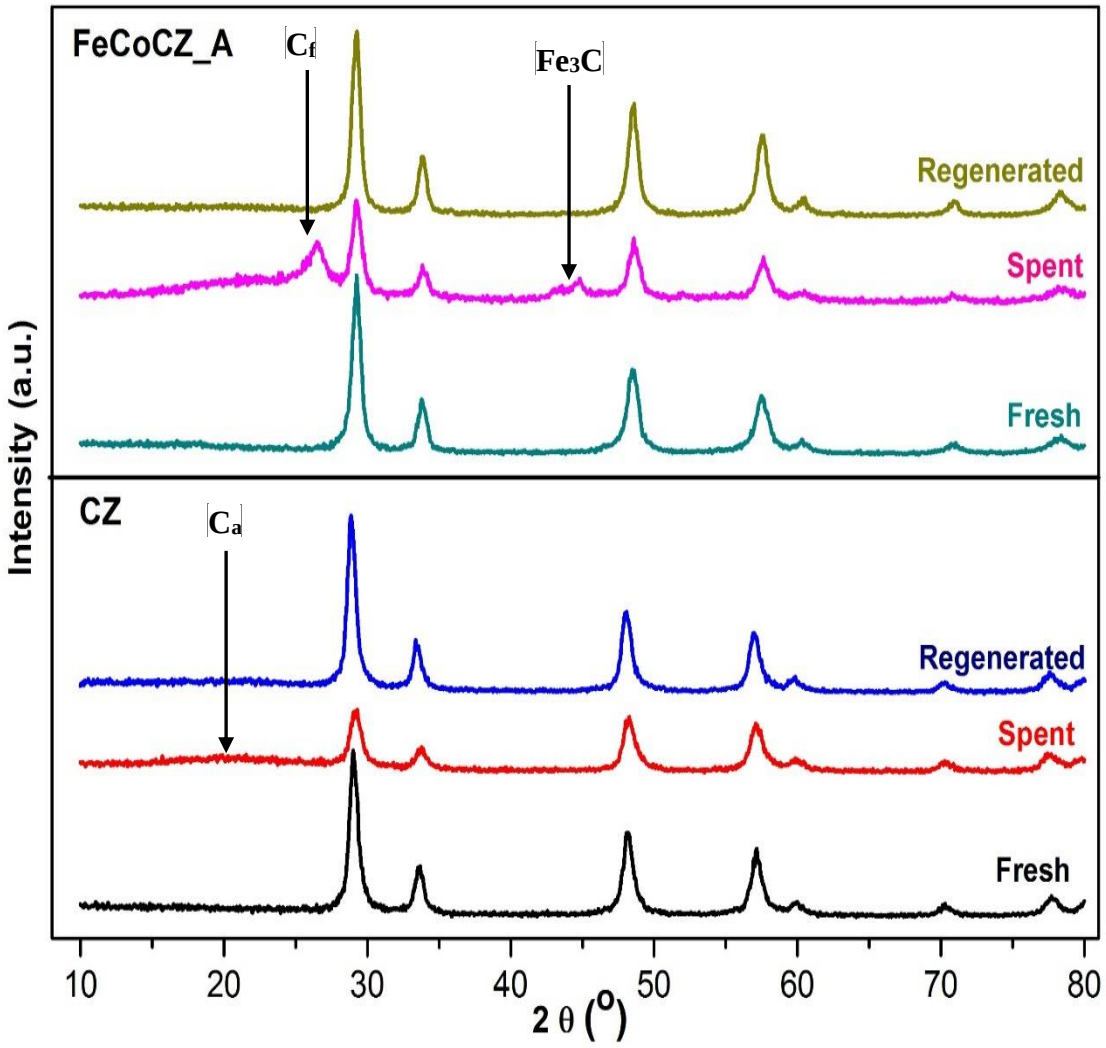

Figure 4.18. XRD patterns of fresh, spent and regenerated samples of CZ and FeCoCZ_A. C_a: amorphous carbon; C_f: filamentous carbon

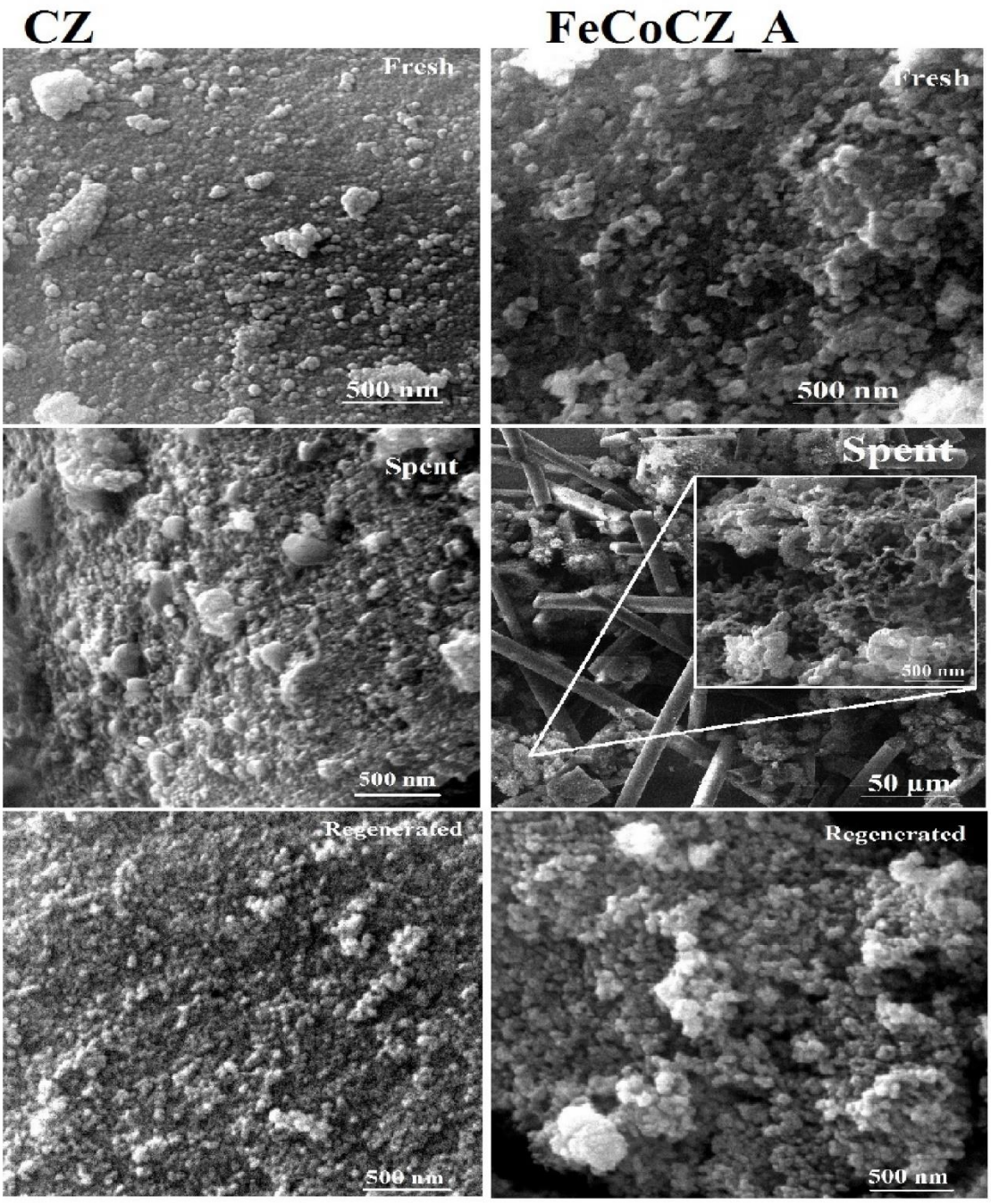

Figure 4.19. FE-SEM micrographs of fresh, spent and regenerated CZ and FeCoCZ_A

Furthermore, for the two regeneration cycles, the regenerated catalyst gave lower total olefin selectivity. This was offset with stability over reaction time-on-stream. C_2 and C_3 olefin selectivity improved with time-on-stream for the two regeneration cycles. Thus, the regenerated catalyst showed appreciable catalytic performance, hence, it has great reusability capacity.

CHAPTER 5

CONCLUSIONS AND RECOMMENDATIONS

5.1 Conclusions.

Cubic-phase Fe-Co co-doped CZ nanocomposites have been successfully synthesized using hydrothermal technique followed by relevant characterization of the obtained nanocomposite samples. Fe and Co were successfully incorporated into the crystal lattice structure of CZ according to the XRD patterns obtained. Improved intrinsic characteristics of ceria-zirconia due to doping with iron and cobalt was obtained and verified by the characterization results. Thus, we can conclude that doping CZ with Fe and Co improves its characteristic properties such as improved physicochemical properties, and enhanced surface acidity and basicity.

The CZ nanocomposite catalysts were tested for hexane cracking. FeCoCZ_A gave the best catalytic performance in terms of cracking conversion, olefin selectivity and stability with relatively high olefin selectivity. Thus, we can conclude that doping CZ with Fe and Co positively influence its catalytic activity and stability for hexane cracking. In addition, higher temperature and lower catalyst weight per feed flowrate (W/F) gave higher n-hexane cracking conversion. However, the results obtained showed that lower temperature favors high propylene selectivity while ethylene selectivity is favored at higher temperature. Also, we infer that the W/F should be greater than 0.065 h since this gave high paraffin yield (56.45 % methane) and selectivity (98.4 % methane). In addition, the spent catalysts were

characterized, analyzed and successfully regenerated by calcination. The regenerated catalyst showed good catalytic performance after two regeneration cycles. Thus, the developed catalyst nanocomposites can be regenerated, maintaining their respective properties with good reusability performance.

5.2 Recommendations.

Further research work can be done to improve this study in terms of catalysts improvement of process optimization, to obtain better desired products distribution. The following recommendations are highlighted for future work:

- Dispersion of the catalyst sample on an acidic support. This will create more acid sites to enhance improved cracking of n-hexane for higher conversion and olefin selectivity.
- Addition of oxygen or steam to aid cracking of n-hexane chains. However, the stability of the catalyst should be monitored although, ceria-based catalysts has mechanical strength to withstand tough reaction conditions.
- Application for heavy oil cracking in supercritical water.

References

[1] M. Hattori and M. Ozawa, “Oxygen storage capacity of ceria alumina composite catalyst for automobile emission control,” vol. 7, pp. 955–956, 2007.

[2] J. R. Kim, W. J. Myeong, and S. K. Ihm, “Characteristics in oxygen storage capacity of ceria-zirconia mixed oxides prepared by continuous hydrothermal synthesis in supercritical water,” *Appl. Catal. B Environ.*, vol. 71, no. 1–2, pp. 57–63, 2007.

[3] Q. Dong, S. Yin, C. Guo, and T. Sato, “Aluminum-doped ceria-zirconia solid solutions with enhanced thermal stability and high oxygen storage capacity,” *Nanoscale Res. Lett.*, vol. 7, no. 1, p. 542, 2012.

[4] T. A. Mehdi Dejhosseini, Tsutomu Aida, Masaru Watanabe, Seiichi Takami, Daisuke Hojo, Nobuaki Aoki, Toshihiko Arita, Atsushi Kishita, “Catalytic Cracking Reaction of Heavy Oil in the Presence of Cerium oxide Nanoparticles in Supercritical Water.pdf,” *ACS J.*, vol. 27, pp. 4624–4631, 2013.

[5] M. Ozawa, K. Matuda, Y. Miura, M. Hattori, T. Okouchi, H. Yuzuriha, T. Sugimoto, and M. Haneda, “Dispersion state and oxygen storage capacity properties of ceria and zirconia nanoparticles supported on alumina by the impregnation process,” *J. Phys. Conf. Ser.*, vol. 379, p. 12014, 2012.

[6] E. Mamontov, T. Egami, R. Brezny, M. Koranne, and S. Tyagi, “Lattice Defects and Oxygen Storage Capacity of Nanocrystalline Ceria and Ceria-Zirconia,” *J. Phys. Chem. B*, vol. 104, no. 47, pp. 11110–11116, 2000.

[7] M. S. H. Asha Gupta, U.V. Waghmare, “Correlation of Oxygen Storage Capacity and Structural Distortion inTransition-Metal-, Noble-Metal-, and Rare-Earth-Ion-Substituted CeO.pdf,” vol. 22, no. 18, pp. 5184–5198, 2010.

[8] T. Yoshikawa, “Oxidative Cracking of Aromatic Compounds Related to Lignin Constituents with Steam Using ZrO2-Al2O3-FeOx Catalyst,” *J. …*, vol. 53, no. 3, pp. 178–183, 2010.

[9] S. M. Schimming, G. S. Foo, O. D. LaMont, A. K. Rogers, M. M. Yung, A. D. D’Amico, and C. Sievers, “Kinetics of hydrogen activation on ceria–zirconia,” *J. Catal.*, vol. 329, pp. 335–347, 2015.

[10] A. M. Hernández-Giménez, D. Lozano-Castelló, and A. Bueno-López, “Effect of CO2, H2O and SO2 in the ceria-catalyzed combustion of soot under simulated diesel exhaust conditions,” *Appl. Catal. B Environ.*, vol. 148–149, pp. 406–414, 2014.

[11] a. Bueno-López, “Diesel soot combustion ceria catalysts,” *Appl. Catal. B Environ.*, vol. 146, pp. 1–11, 2014.

[12] K. Shimizu, H. Kawachi, S. Komai, K. Yoshida, Y. Sasaki, and A. Satsuma, "Carbon oxidation with Ag/ceria prepared by self-dispersion of Ag powder into nano-particles," *Catal. Today*, vol. 175, no. 1, pp. 93–99, 2011.

[13] K. Yamazaki, Y. Sakakibara, F. Dong, and H. Shinjoh, "The remote oxidation of soot separated by ash deposits via silver–ceria composite catalysts," *Appl. Catal. A Gen.*, vol. 476, pp. 113–120, 2014.

[14] T. N. Ravishankar, T. Ramakrishnappa, G. Nagaraju, and H. Rajanaika, "Synthesis and Characterization of CeO_2 Nanoparticles via Solution Combustion Method for Photocatalytic and Antibacterial Activity Studies," *ChemistryOpen*, vol. 4, no. 2, pp. 146–154, 2015.

[15] K. Shimizu, H. Kawachi, and A. Satsuma, "Study of active sites and mechanism for soot oxidation by silver-loaded ceria catalyst," *Appl. Catal. B Environ.*, vol. 96, no. 1–2, pp. 169–175, 2010.

[16] C. de Leitenburg, A. Trovarelli, J. Llorca, F. Cavani, and G. Bini, "The effect of doping CeO2 with zirconium in the oxidation of isobutane," *Appl. Catal. A Gen.*, vol. 139, no. 1–2, pp. 161–173, 1996.

[17] G. C. Pontelli, R. P. Reolon, A. K. Alves, F. A. Berutti, and C. P. Bergmann, "Application of cerium oxide electrospun fibers in the catalytic combustion of methane," *Appl. Catal. A Gen.*, vol. 405, no. 1–2, pp. 79–83, 2011.

[18] T. Murota, T. Hasegawa, S. Aozasa, H. Matsui, and M. Motoyama, "Production method of cerium oxide with high storage capacity of oxygen and its mechanism," *J. Alloys Compd.*, vol. 193, no. 1–2, pp. 298–299, 1993.

[19] P. Fornasiero, "Rh-Loaded CeO2-ZrO2 Solid-Solutions as Highly Efficient Oxygen Exchangers: Dependence of the Reduction Behavior and the Oxygen Storage Capacity on the Structural-Properties," *Journal of Catalysis*, vol. 151, no. 1. pp. 168–177, 1995.

[20] H. X. Mai, L. D. Sun, Y. W. Zhang, R. Si, W. Feng, H. P. Zhang, H. C. Liu, and C. H. Yan, "Shape-selective synthesis and oxygen storage behavior of ceria nanopolyhedra, nanorods, and nanocubes," *J. Phys. Chem. B*, vol. 109, no. 51, pp. 24380–24385, 2005.

[21] A. Morikawa, T. Suzuki, T. Kanazawa, K. Kikuta, A. Suda, and H. Shinjo, "A new concept in high performance ceria-zirconia oxygen storage capacity material with Al2O3 as a diffusion barrier," *Appl. Catal. B Environ.*, vol. 78, no. 3–4, pp. 210–221, 2008.

[22] H. Konno, T. Okamura, T. Kawahara, Y. Nakasaka, T. Tago, and T. Masuda, "Kinetics of n-hexane cracking over ZSM-5 zeolites - Effect of crystal size on effectiveness factor and catalyst lifetime," *Chem. Eng. J.*, vol. 207–208, pp. 490–496, 2012.

[23] C. Boyadjian, B. Van Der Veer, I. V. Babich, L. Lefferts, and K. Seshan, "Catalytic oxidative cracking as a route to olefins: Oxidative conversion of hexane over MoO3-Li/MgO," *Catal. Today*, vol. 157, no. 1–4, pp. 345–350, 2010.

[24] Y. Wang, T. Yokoi, S. Namba, J. N. Kondo, and T. Tatsumi, "Catalytic cracking of n-hexane for producing propylene on MCM-22 zeolites," *Appl. Catal. A Gen.*, vol. 504, pp. 192–202, 2015.

[25] W. O. Haag, R. M. Dessau, and R. M. Lago, "Kinetics and Mechanism of Paraffin Cracking with Zeolite Catalysts," *Stud. Surf. Sci. Catal.*, vol. 60, no. C, pp. 255–265, 1991.

[26] A. F. H. Wielers, M. Vaarkamp, and M. F. M. Post, "Relation between properties and performance of zeolites in paraffin cracking," *J. Catal.*, vol. 127, no. 1, pp. 51–66, 1991.

[27] F. Deganello and a Martorana, "Phase analysis and oxygen storage capacity of ceria-lanthana- based TWC promoters prepared by sol-gel routes," *J. Solid State Chem.*, vol. 163, no. 2, pp. 527–533, 2002.

[28] J.-R. Kim, W.-J. Myeong, and S.-K. Ihm, "Characteristics of CeO2–ZrO2 mixed oxide prepared by continuous hydrothermal synthesis in supercritical water as support of Rh catalyst for catalytic reduction of NO by CO," *J. Catal.*, vol. 263, no. 1, pp. 123–133, 2009.

[29] M. Pudukudy and Z. Yaakob, "Catalytic aspects of ceria-zirconia solid solution : Part-I An update in the synthesis , properties and chemical reactions of ceria zirconia solid solution Manoj Pudukudy and Zahira Yaakob," *Der Pharma Chem.*, vol. 6, no. 1, pp. 188–216, 2014.

[30] G. Chen, F. Rosei, and D. Ma, "Template engaged synthesis of hollow ceria-based composites," *Nanoscale*, vol. 7, no. 13, pp. 5578–5591, 2015.

[31] B. Zhu and M. D. Mat, "Studies on dual phase ceria-based composites in electrochemistry," *Int. J. Electrochem. Sci.*, vol. 1, pp. 383–402, 2006.

[32] E. J. Salazar-sandoval, "Ceria Nanoparticle Hybrid Materials : Interfacial Design and Structure Control," 2015.

[33] X. Yin, Y. Zhang, Z. Fang, Z. Xu, and W. Zhu, "Hydrothermal synthesis of CeO2 nanorods using a strong base–weak acid salt as the precipitant," *Nanosci. Methods*, vol. 1, no. October, pp. 115–122, 2012.

[34] Q. Yuan, H.-H. Duan, L.-L. Li, L.-D. Sun, Y.-W. Zhang, and C.-H. Yan, "Controlled synthesis and assembly of ceria-based nanomaterials," *J. Colloid Interface Sci.*, vol. 335, no. 2, pp. 151–167, 2009.

[35] N. A. Tapan, U. B. Cacan, and D. Varışlı, "Ceria Based Nano-composite Synthesis for Direct Alcohol Fuel Cells," *Int. J. Electrochem. Sci.*, vol. 9, pp. 4440–4464, 2014.

[36] X. Zhang, Q. Wang, J. Zhang, J. Wang, M. Guo, S. Chen, C. Li, C. Hu, and Y. Xie, "One step hydrothermal synthesis of CeO $_2$ –ZrO $_2$ nanocomposites and investigation of the morphological evolution," *RSC Adv.*, vol. 5, no. 109, pp. 89976–89984, 2015.

[37] M. Hirano and E. Kato, "Hydrothermal synthesis of Cerium(IV) oxide," *J. Am. Ceram. Soc.*, vol. 79, no. 3, pp. 777–780, 1996.

[38] Z. Wang and X. Feng, "Polyhedral shapes of CeO2 nanoparticles," *J. Phys. Chem. B*, vol. 107, pp. 13563–13566, 2003.

[39] T. Tsoncheva, R. Ivanova, J. Henych, M. Dimitrov, M. Kormunda, D. Kovacheva, N. Scotti, V. Dal, and V. Stengl, "Effect of preparation procedure on the formation of nanostructured ceria – zirconia mixed oxide catalysts for ethyl acetate oxidation : Homogeneous precipitation with urea vs template-assisted hydrothermal synthesis," *Appl. Catal. A Gen.*, vol. 502, no. 5, pp. 418–432, 2015.

[40] S. Machmudah, M. Akmal Hadian, L. Samodro K., S. Winardi, _ W., H. Kanda, and M. Goto, "Preparation of Ceria-Zirconia Mixed Oxide by Hydrothermal Synthesis," *Mod. Appl. Sci.*, vol. 9, no. 7, pp. 134–139, 2015.

[41] L. Pang, X. Wang, and X. Tang, "Ceria Nanotube Formed by Sacrificed Precursors Template through Oswald Ripening," *PLoS One*, vol. 10, no. 7, p. e0132536, 2015.

[42] K. Houlberg, E. D. Bøjesen, C. Tyrsted, A. Mamakhel, X. Wang, R. Su, F. Besenbacher, and B. B. Iversen, "Hydrothermal Synthesis and in Situ Powder X-ray Diffraction Study of Bismuth-Substituted Ceria Nanoparticles," *Cryst. Growth Des.*, vol. 15, no. 8, pp. 3628–3636, 2015.

[43] H. S. Potdar, S. B. Deshpande, a S. Deshpande, S. P. Gokhale, S. K. Date, Y. B. Khollam, and a J. Patil, "Preparation of ceria–zirconia (Ce< sub> 0.75</sub> Zr< sub> 0.25</sub> O< sub> 2</sub>) powders by microwave–hydrothermal (MH) route," *Mater. Chem. Phys.*, vol. 74, pp. 306–312, 2002.

[44] F. Zhang, C.-H. Chen, J. C. Hanson, R. D. Robinson, I. P. Herman, and S.-W. Chan, "Phases in Ceria-Zirconia Binary Oxide (1-x)CeO2-xZrO2 Nanoparticles: The Effect of Particle Size," *J. Am. Ceram. Soc.*, vol. 89, no. 3, pp. 1028–1036, 2006.

[45] B. Kaemena, S. D. Senanayake, A. Meyer, J. T. Sadowski, J. Falta, and J. I. Flege, "Growth and Morphology of Ceria on Ruthenium (0001)," *J. Phys. Chem. C*, vol. 117, no. 1, pp. 221–232, 2013.

[46] G. R. Patzke, F. Krumeich, and R. Nesper, "Oxidic nanotubes and nanorods - Anisotropic modules for a future nanotechnology," *Angew. Chemie - Int. Ed.*, vol. 41, pp. 2446–2461, 2002.

[47] S. Gnanam and V. Rajendran, "Influence of Various Surfactants on Size ,

Morphology , and Optical Properties of CeO 2 Nanostructures via Facile Hydrothermal Route," *J. Nanomater.*, vol. 2013, 2013.

[48] M. Y. Cui, J. X. He, N. P. Lu, Y. Y. Zheng, W. J. Dong, W. H. Tang, B. Y. Chen, and C. R. Li, "Morphology and size control of cerium carbonate hydroxide and ceria micro/nanostructures by hydrothermal technology," *Mater. Chem. Phys.*, vol. 121, no. 1–2, pp. 314–319, 2010.

[49] S. Wang, L. Zhao, W. Wang, Y. Zhao, G. Zhang, X. Ma, and J. Gong, "Morphology control of ceria nanocrystals for catalytic conversion of CO2 with methanol.," *Nanoscale*, vol. 5, pp. 5582–8, 2013.

[50] Y. Minamidate, S. Yin, and T. Sato, "Synthesis of Monodispersed rod-like and spherical CeO 2 particles by mild solution process," *IOP Conf. Ser. Mater. Sci. Eng.*, vol. 1, p. 12003, 2009.

[51] L. F. Liotta, G. Pantaleo, a. Macaluso, G. Marcì, S. Gialanella, and G. Deganello, "Ceria-Zirconia Nanostructured Materials for Catalytic Applications: Textural Characteristics and Redox Properties," *J. Sol-Gel Sci. Technol.*, vol. 28, pp. 119–132, 2003.

[52] J. R. Kim, K. Y. Lee, M. J. Suh, and S. K. Ihm, "Ceria-zirconia mixed oxide prepared by continuous hydrothermal synthesis in supercritical water as catalyst support," *Catal. Today*, vol. 185, no. 1, pp. 25–34, 2012.

[53] J. Kullgren, K. Hermansson, and P. Broqvist, "Supercharged low-temperature oxygen storage capacity of ceria at the nanoscale," *J. Phys. Chem. Lett.*, vol. 4, no. 4, pp. 604–608, 2013.

[54] S. Meiqing, W. Xinquan, A. Yuan, W. Duan, Z. Minwei, and W. Jun, "Dynamic Oxygen Storage Capacity Measurements on Ceria-Based Material," *J. Rare Earths*, vol. 25, no. 1, pp. 48–52, 2007.

[55] N. M. M. Venkatesh, S.Z. Mohamed, "Effective synthesis of quinoxalines over ceria based solid acids coated on honeycomb monoliths," *Indian J. Chem.*, vol. 54, no. July, pp. 843–850, 2015.

[56] D. Stošić, S. Bennici, J. L. Couturier, J. L. Dubois, and A. Auroux, "Influence of surface acid-base properties of zirconia and titania based catalysts on the product selectivity in gas phase dehydration of glycerol," *Catal. Commun.*, vol. 17, pp. 23–28, 2012.

[57] L. Vivier and D. Duprez, "Ceria-Based Solid Catalysts for Organic Chemistry," *ChemSusChem*, vol. 3, no. 6, pp. 654–678, 2010.

[58] X. Ge, S. Hu, and Q. Sun, "Surface Acidity/Basicity and Catalytic Reactivity of CeO2/ -Al2O3 Catalysts for the Oxidative Dehydrogenation of Ethane with Carbon Dioxide to Ethylene.pdf," *J. Nat. Gas Chem.*, vol. 12, no. 3, pp. 119–122, 2003.

[59] K. C. Petallidou, K. Polychronopoulou, and A. M. Efstathiou, "Novel Catalytic Systems for Hydrogen Production via the Water-Gas Shift Reaction," *Conf. Pap. Energy*, vol. 2013, pp. 1–8, 2013.

[60] S. Sugunan and C. R. K. Seena, "Acidity/basicity, electron donor properties and catalytic activity of sulphate modified ceria," *Indian J. Chem.*, vol. 38A, no. November, pp. 1123–1128, 1999.

[61] H. Wang, S. Gao, F. Yu, Y. Liu, X. Weng, and Z. Wu, "Effective Way to Control the Performance of a Ceria-Based DeNO $_x$ Catalyst with Improved Alkali Resistance: Acid–Base Adjusting," *J. Phys. Chem. C*, vol. 119, no. 27, pp. 15077–15084, 2015.

[62] S. Damyanova, B. Pawelec, K. Arishtirova, M. V. M. Huerta, and J. L. G. Fierro, "Study of the surface and redox properties of ceria-zirconia oxides," *Appl. Catal. A Gen.*, vol. 337, no. 1, pp. 86–96, 2008.

[63] E. Aneggi, M. Boaro, C. De Leitenburg, G. Dolcetti, and A. Trovarelli, "Insights into the redox properties of ceria-based oxides and their implications in catalysis," *J. Alloys Compd.*, vol. 408–412, pp. 1096–1102, 2006.

[64] I. Alessandri, M. A. Bañares, L. E. Depero, M. Ferroni, P. Fornasiero, F. C. Gennari, N. Hickey, M. V. Martinez-Huerta, and T. Montini, "Structural investigation of Ce2Zr2O8 after redox treatments which lead to low temperature reduction," *Top. Catal.*, vol. 41, no. 1–4, pp. 35–42, 2006.

[65] D. Prasada and J. Leea, "Chemical synthesis and characterization of CexZr1-xO2 powders by a modified sol-gel method," *J. Ceram. ...*, vol. 10, no. 6, pp. 748–752, 2009.

[66] C. Liang, J. Qiu, Z. Li, and C. Li, "Synthesis of nanostructured ceria, zirconia and ceria–zirconia solid solutions using an ultrahigh surface area carbon material as a template," *Nanotechnology*, vol. 15, no. 7, pp. 843–847, 2004.

[67] L. Katta, P. Sudarsanam, G. Thrimurthulu, and B. M. Reddy, "Doped nanosized ceria solid solutions for low temperature soot oxidation: Zirconium versus lanthanum promoters," *Appl. Catal. B Environ.*, vol. 101, no. 1–2, pp. 101–108, 2010.

[68] A. Trovarelli, "Structural Properties and Nonstoichiometric Behavior of CeO~ 2," *Catal. Sci. Ser.*, vol. 2, pp. 15–46, 2002.

[69] M. Thammachart, V. Meeyoo, T. Risksomboon, and S. Osuwan, "Catalytic activity of CeO 2 – ZrO 2 mixed oxide catalysts prepared via sol – gel technique : CO oxidation," *Catal. Today*, vol. 68, no. 1–3, pp. 53–61, 2001.

[70] J. R. Sohn, S. H. Lee, and J. S. Lim, "New solid superacid catalyst prepared by doping ZrO2 with Ce and modifying with sulfate and its catalytic activity for acid catalysis," *Catal. Today*, vol. 116, pp. 143–150, 2006.

[71] J. Wang, M. Shen, J. Wang, J. Gao, J. Ma, and S. Liu, “Effect of cobalt doping on ceria-zirconia mixed oxide: Structural characteristics, oxygen storage/release capacity and three-way catalytic performance,” *J. Rare Earths*, vol. 30, no. 9, pp. 878–883, 2012.

[72] J. Wang, B. Zhang, M. Shen, J. Wang, W. Wang, J. Ma, S. Liu, and L. Jia, “Effects of Fe-doping of ceria-based materials on their microstructural and dynamic oxygen storage and release properties,” *J. Sol-Gel Sci. Technol.*, vol. 58, no. 1, pp. 259–268, 2011.

[73] B. M. Reddy, P. Bharali, G. Thrimurthulu, P. Saikia, L. Katta, and S. E. Park, “Catalytic efficiency of ceria-zirconia and ceria-hafnia nanocomposite oxides for soot oxidation,” *Catal. Letters*, vol. 123, no. 3–4, pp. 327–333, 2008.

[74] O. H. Laguna, A. Pérez, M. A. Centeno, and J. A. Odriozola, “Synergy between gold and oxygen vacancies in gold supported on Zr-doped ceria catalysts for the CO oxidation,” *Appl. Catal. B Environ.*, vol. 176–177, pp. 385–395, 2015.

[75] O. H. Laguna, M. A. Centeno, M. Boutonnet, and J. A. Odriozola, “Fe-doped ceria solids synthesized by the microemulsion method for CO oxidation reactions,” *Appl. Catal. B Environ.*, vol. 106, no. 3–4, pp. 621–629, 2011.

[76] O. H. Laguna, F. Romero Sarria, M. A. Centeno, and J. A. Odriozola, “Gold supported on metal-doped ceria catalysts (M = Zr, Zn and Fe) for the preferential oxidation of CO (PROX),” *J. Catal.*, vol. 276, no. 2, pp. 360–370, 2010.

[77] M. Kang, X. Wu, J. Zhang, N. Zhao, W. Wei, and Y. Sun, “Enhanced thermochemical CO2 splitting over Mg- and Ca-doped ceria/zirconia solid solutions,” *RSC Adv.*, pp. 5583–5590, 2013.

[78] N. Hosseinpour, A. A. Khodadadi, Y. Mortazavi, and A. Bazyari, “Nano-ceria-zirconia promoter effects on enhanced coke combustion and oxidation of CO formed in regeneration of silica-alumina coked during cracking of triisopropylbenzene,” *Appl. Catal. A Gen.*, vol. 353, no. 2, pp. 271–281, 2009.

[79] Y. Zhang, L. Zhang, J. Deng, H. Dai, and H. He, “Controlled Synthesis, Characterization, and Morphology-Dependent Reducibility of Ceria-Zirconia-Yttria Solid Solutions with Nanorod-like , Microspherical , Microbowknot-like , and Micro-octahedral Shapes 2181,” *Inorg. Chem.*, vol. 48, no. 5, pp. 2181–2192, 2009.

[80] M. Golmohammadi, S. J. Ahmadi, and J. Towfighi, “Catalytic cracking of heavy petroleum residue in supercritical water: Study on the effect of different metal oxide nanoparticles,” *J. Supercrit. Fluids*, vol. 113, pp. 136–143, 2016.

[81] V. S. Escribano, C. del Hoyo Martínez, E. Fernández López, J. M. Gallardo Amores, and G. Busca, “Characterization of a ceria-zirconia-supported Cu oxides catalyst: An FT-IR study on the catalytic oxidation of propylene,” *Catal. Commun.*, vol. 10, no. 6, pp. 861–864, 2009.

[82] G. Busca, “Spectroscopic Characterization of the Acid Properties of Metal Oxide Catalysts,” *Catal. Today*, vol. 41, no. 1–3, pp. 191–206, 1998.

[83] M. I. Zaki, M. a. Hasan, F. a. Al-Sagheer, and L. Pasupulety, “In situ FTIR spectra of pyridine adsorbed on SiO_2-Al_2O_3, TiO_2, ZrO_2 and CeO_2: General considerations for the identification of acid sites on surfaces of finely divided metal oxides,” *Colloids Surfaces A Physicochem. Eng. Asp.*, vol. 190, no. 3, pp. 261–274, 2001.

[84] Y. Zhang, L. Zhang, J. Deng, H. Dai, and H. He, “Controlled Synthesis, Characterization, and Morphology-Dependent Reducibility of Ceria-Zirconia-Yttria Solid Solutions with Nanorod-like, Microspherical, Microbowknot-like, and Micro-octahedral Shapes,” *Inorg. Chem.*, vol. 48, no. 5, pp. 2181–2192, 2009.

[85] R. Terry and K. Baker, “Coking problems associated with hydrocarbon conversion processes,” *ACS Div. Fuel Chem. Prepr.*, vol. 41, no. 2, pp. 521–523, 1996.

[86] R. T. K. Baker, M. A. Barber, P. S. Harris, F. S. Feates, and R. J. Waite, “Nucleation and growth of carbon deposits from the nickel catalyzed decomposition of acetylene,” *J. Catal.*, vol. 26, no. 1, pp. 51–62, 1972.

Vitae

Name	:Oluwole Olagoke AJUMOBI
Nationality	:Nigerian
Date of Birth	:10/30/1987
Email	:oluwole.ajumobi@gmail.com
Address	:21 Ayo Buhari, Igboho, Alapere, Ketu, Lagos, Nigeria.
Academic Background	:B.Sc. Chemical Engineering, O.A.U, Ile-Ife.

Profile

An eloquent, versatile, and result-oriented individual, with a pragmatic approach towards delivering solutions to both managerial and technical problems, building a desired path towards a valuable engineering career.

Skill Set

- Microsoft Office Suite: Word, Excel, Power-Point
- Mathematica
- Matlab

Education and Training

Master's Degree: Chemical Engineering, 2017

King Fadh University of Petroleum and Minerals (KFUPM) – Dhahran, Dammam, Saudi Arabia.

- Courses in Advanced Thermodynamics, Transport Phenomena, Advanced Mathematics for Engineers, Advanced Reaction Engineering, Heterogeneous Catalysis, Numerical Analysis, Polymer Nanocomposites, Independent Research.
- **Thesis: Development of Ceria-based Nanocomposites/Catalysts for Hydrocarbon Cracking**.
  - Catalyst Synthesis ($Ce_{1-x}Zr_xO_2$, $0.2<x<0.3$) using Hydrothermal Technique
  - Sample characterization and Analysis
  - Catalytic cracking of hexane and heavy oil upgrading in superheated steam

Bachelor's Degree (Second Class Upper Division): Chemical Engineering, 2012

Obafemi Awolowo University, Ile-Ife, Osun State.

- Thesis: Adsorption of Ethanol-Water Mixture using Activated Sawdust.

West Africa Senior School Certificate Examination (WASSCE): Sciences, 2004
United Secondary School, Ijokodo, Ibadan, Oyo State.

Publication

- Boron-doped activated carbon as efficient and selective adsorbent for ultra-deep desulfurization of 4,6-dimethyldibenzothiophene, Chem. Eng. J. (2017). doi:10.1016/j.cej.2017.03.132.
- Synthesis of Iron- and cobalt-doped ceria-zirconia nanocomposites and their novel application for catalytic cracking of n-hexane with regenerative capability (under review).
- Application of ceria-based catalysts for upgrading oil sand bitumen in superheated steam condition (under review).

Work Experience

Industrial Training Intern

August 2010 – January 2011
Eagle Paints Nigeria Limited, Agidingbi, Ikeja, Lagos State

- Assisted the chemical manager in measurement of the different chemicals in appropriate proportion for the manufacture of various types of paints in the factory.
- Laboratory analysis of the raw materials used in the production of the paints.
- Quality control analysis on different paint products produced from the factory such as specific gravity, viscosity, color match tests, and opacity determination.

Industrial Training Intern

March –April 2010
Opa Dam Water Works, Obafemi Awolowo University, Ile-Ife, Osun state.
JOB FUNCTIONS

- Monitored the several processes and activities at the water treatment plant.
- Performed various quality control tests on water (i.e. chlorine test, ph. Test, salt test).

Achievements

- Being the president of NDLEA CDS group (NYSC), I lead a program involving dissemination of legal information on drug use and abuse to secondary and tertiary school students in Jalingo.
- Part of a team of individuals who aided significant improvement in the grades of new students by performing free tutorials for first year students

Conferences Attended

- 15th Workshop (Jan, 2016), Center for Excellence for Scientific Research Collaboration with MIT
  Theme: Clean Water Energy"
- 25th Annual Saudi-Japan Symposium (Dec, 2015)
  Theme: "Catalysts in Petroleum Refining and Petrochemicals"
- Nigerian Society of Chemical Engineers, 15th National Conference 2012,
  Theme: "Entrepreneurship, Technology and Chemical Engineering in the Revitalization of the Nigerian Economy"

Awards

- Full Post Graduate Scholarship for Chemical Engineering 2014 by KFUPM, Saudi Arabia
- Federal Government Of Nigeria Undergraduate Scholarship, Federal Scholarship Board (2009-2011)
- Ekiti State Scholarship by Ekiti State Scholarship and Education Board (2009)

Leadership Positions Held

- Community Development Service, President NDLEA Group, Ardo-Kola, Taraba state, 2013.
- Alumni President 2012 set, CFI
- Final year brethren project coordinator, CFI (2011)
- Academic Counsellor, Charis Fellowship International, OAU (CFI) 2008-2010

Affiliations

- Nigeria Society of Engineers

Hobbies

Sports, meeting people, entertainment, and engaging in intellectual discussions.

Referees

- Available on Request